



WICHITA STATE  
UNIVERSITY

UNIVERSITY LIBRARIES

## Detection and classification of cerebral vascular injury via microwave sensing and AI

Item Type	Thesis
Authors	Jensen, Reilly Shawn
Publisher	Wichita State University
Rights	© Copyright 2025 by Reilly Jensen All Rights Reserve
Download date	2026-05-17 23:31:11
Link to Item	<a href="https://hdl.handle.net/10057/30342">https://hdl.handle.net/10057/30342</a>

DETECTION AND CLASSIFICATION OF CEREBRAL VASCULAR INJURY VIA MICROWAVE  
SENSING AND AI

Thesis by

Reilly Shawn Jensen

Bachelor of Science, Kansas State University, 2021

Bachelor of Arts, Kansas State University, 2021

Submitted to the Department of Biomedical Engineering  
and the faculty of the Graduate School of  
Wichita State University  
in partial fulfillment of  
the requirements for the degree of  
Master of Science

July 2025

© Copyright 2025 by Reilly Jensen

All Rights Reserve

DETECTION AND CLASSIFICATION OF CEREBRAL VASCULAR INJURY VIA MICROWAVE  
SENSING AND AI

The following faculty members have examined the final copy of this thesis for form and content, and recommend that it be accepted in partial fulfillment of the requirement for the degree of Master of Science with a major in Biomedical Engineering.

Kim Cluff, Committee Chair

Yongkuk Lee, Committee Member

Shruti Kshirsagar, Committee Member

## ABSTRACT

This thesis evaluates the capability of a monostatic RFR in detecting physiological changes which accommodate cerebral hemorrhage. The expected result is that the data collected from the RFR can be used in the training of machine learning models which can then accurately predict the flow rate of hemorrhage. The second chapter of this thesis is dedicated to a literature review covering the following: The physiology of hemorrhagic stroke, alternative monitoring methods and their underlying theories and applications, current obstacles and future works. The third chapter summarizes the methods and results of the dataset generation and artificial intelligence model development and performance.

This study used an *ex vivo* porcine model. Radio frequency sweeps were conducted using a vector network analyzer. The machine learning models used were: linear regression, logistic regression, random forest, k-nearest neighbors. Several convolutional neural network models were explored. Hyperparameter searches were conducted, and the best performing models were evaluated. It was concluded that linear regression and logistic regression failed to predict flow rate based on resonant frequency shifts. Both the k-nearest neighbors and random forest models performed well, achieving 81.1% and 74.2% accuracy, respectively. Finally, the results for the convolutional neural networks were inconclusive due to insufficient dataset size.

## TABLE OF CONTENTS

Chapter	Page
I. INTRODUCTION	1
Overview of Cerebral Hemorrhage.....	1
Problem Statement .....	2
Aims .....	2
REFERENCES.....	4
II. LITERATURE REVIEW	6
Background.....	6
Pathophysiology of Hemorrhagic stroke .....	6
Alternative Monitoring Methods .....	20
References.....	31
Table of referenced Studies .....	38
References.....	48
III. CLASSIFICATION OF THE RATE OF GROWTH OF A PHANTOM CEREBRAL HEMORRHAGE IN AN EX VIVO PORCINE MODEL VIA A RADIO FREQUENCY RESONATOR	52
Abstract.....	52
Introduction.....	52
Methods.....	54
Results.....	70
Discussion .....	80
References.....	83

## LIST OF TABLES

Table		Page
1.	Table of reference for all studies referred to in the literature review .....	38
2.	Anatomical metrics of each replicant.....	58
3.	Hyperparameters explored and their values.....	66
4.	Summary of results from the linear regression models .....	70
5.	Summary of the parameters explored, the best parameters found, and accuracy associated with the best parameter configuration per model.....	71
6.	Optimal hyperparameter configuration for the single layer CNN model of both the 10 sweep and 20 sweep length datasets .....	75
7.	Optimal hyperparameter configuration for the 2 layers CNN model of both the 10 sweep and 20 sweep length datasets .....	75
8.	Optimal hyperparameter configuration for the 3 layers CNN model of both the 10 sweep and 20 sweep length datasets .....	75

## LIST OF FIGURES

Figure		Page
1.	An illustration of the brain from Andrea Vesalius's <i>De humani corporis fabrica</i> (Vesalius 1543). Image Courtesy of the National Library of Medicine. ....	8
2.	Portrait of Daniel Lambert (1770–1809), known for his exceptional corpulence. Artist: Unknown. Image courtesy of the Wellcome Collection. CC BY 4.0 (Unknown 1809) ....	11
3.	Comparison of location between ICH and SH, Courtesy of (Morais Filho, Rego et al. 2021) .....	12
4.	Comparison of lobar (A) vs deep (B) ICH, courtesy of (Mendiola, Arboix et al. 2023)..	13
5.	Progression of atherosclerosis. Courtesy of (YitzhakNat 2022). ....	15
6.	Risk factors such as smoking, atherosclerosis, hypertension and genetic predisposition contribute to inflammatory pathways which result in cerebral aneurysm formation and rupture. Courtesy of (Chalouhi, Hoh et al. 2013). ....	16
7.	(a) Blood escapes from the initial rupture (red arrows), causing early hematoma formation (dashed circle) with minimal tissue counter-pressure (black arrows). (b) Hematoma growth increases pressure, stretching surrounding vessels (blue line). (c) Press .....	18
8.	First image created via EIT (a) and a representative cross-section of a forearm (b), courtesy of (Brown and Barber 1982).....	21
9.	Electrodes are placed around the object of interest. A current source is applied to the transmitting electrodes, and the voltage output is measured at the receiving electrodes. Courtesy of (Tiwari, Meribout et al. 2023). ....	22
10.	Vector representation of the relationship between the initial magnetic field $B_0$ , the induced field $\theta B$ , the resultant magnetic field $B_T$ , and the phase shift $\theta\psi$ . ....	25
11.	The loop trace, spiral trace, trace gas, and the gap between the gap along the spiral measure 2 mm, 1.5 mm, 0.5 mm, and 1 mm respectively. There are nine turns within the spiral pattern.....	55
12.	The sensor is held in place by a cloth band which wraps around the head (a). The experimental set up consisting of the tubing kit and syringe injector (b). ....	58
13.	Starting from the apex of the head, 5 positions are marked 5 cm apart along the mid-sagittal plane. ....	59
14.	A linear model is fit for the second resonant frequency (x-axis) and total volume (y-axis) ( $R^2 = 0.967$ ). A leftward shift in the resonant frequency is observed as volume increases. ....	60

LIST OF FIGURES (continued)

Figure	Page
15. Time-frequency images are created of the imaginary component, magnitude, and phase (a). These features form the 3 channels of the inputted hypercubes which serve as samples for each flow rate (b).....	62
16. The architecture consists of a single convolutional layer (yellow) followed by a maxpooling layer (orange). A flattening layer (purple) and two dense-dropout (purple-black) precede the output (dark purple). .....	64
17. A second convolutional-maxpooling layer is added to the architecture. ....	65
18. Finally, a third convolutional-maxpooling layer is considered.....	65
19. Training accuracy and loss of each CNN model for 10 sweep length time-frequency images. ....	68
20. Training accuracy and loss of each CNN model for 20 sweep length time-frequency images. ....	69
21. The confusion matrix of the highest performing fold of the logistic regression model (a) and its accompanying ROC curve (AUC = 0.61) (b). The grand mean ( $X$ ) and standard deviation ( $\sigma$ ) of the k-stratified fold accuracy (k=10) are 28.0% and 0.90%, respectively. ....	72
22. The confusion matrix of the highest performing fold of the random forest model (a) and its accompanying ROC curve (AUC = 0.94) (b). The grand mean ( $X$ ) and standard deviation ( $\sigma$ ) of the k-stratified fold accuracy (k=10) are 74.2% and 0.97%, respectively .....	73
23. The confusion matrix of the highest performing fold of the KNN model (a) and its accompanying ROC curve (AUC = 0.96) (b). The grand mean ( $X$ ) and standard deviation ( $\sigma$ ) of the k-stratified fold accuracy (k=10) are 81.1% and 0.58%, respectively.....	74
24. Confusion matrices of each CNN model for both the 10 and 20 sweep length datasets. .	77
25. Stratified k-fold accuracy for each CNN model-database pair. ....	79
26. ROC curves for each model-dataset pair.....	80

# CHAPTER I

## INTRODUCTION

### Overview of Cerebral Hemorrhage

Cerebral hemorrhage (CH) is caused by traumatic and vascular complications, and is one of the leading causes of death and disability world-wide (Magid-Bernstein et al. 2022). The mechanistic underpinnings of hematoma formation within the context of cerebral vascular complications (hemorrhagic stroke) are still poorly understood; however, a handful of case studies supplemented by animal models have given some insight (Edlow et al. 2012; Brott et al. 1997; Liu et al. 2015).

The initial stage of hematoma formation displays a growth period to a baseline volume within the first few hours after onset. After the initial growth period, a secondary growth phase may follow. The risk factors for this secondary phase are initial hematoma volume, rate of growth, and state of coagulation (Brouwers and Greenberg 2013). The importance of predicting the occurrence of secondary growth is exemplified by the 10% increase in mortality associated with every 5% increase in hematoma volume. Additionally, every milliliter increase in volume increases the chance of severe disability as a health outcome by 7% (LoPresti et al. 2014).

Currently, the most widely accepted model for CH onset and secondary expansion proposes that an initial bleed from a single vessel rupture contributes to initial hematoma formation. The forces associated with the expansion of this initial hematoma contribute to the development of secondary expansion caused by the rupturing of the surrounding vasculature. The potential for

secondary and tertiary vessel ruptures increases indirectly with distance from the initial hematoma (Schlunk and Greenberg 2015).

## Problem Statement

Perhaps the most important factor for positive health outcomes for stroke patients is the time from the onset of the stroke to treatment. Current methods for detecting and classifying strokes, such as field triage scores, computed tomography, and magnetic resonance imaging, are less than ideal with regards to sensitivity, accuracy, and expediency. Although typically considered the gold standard along with MRI, CT scans have lower sensitivity within the first few hours after onset. MRI and angio-specific CT methods call for time-consuming protocols and image processing, resulting in further brain tissue death (Patil et al. 2022; Marler et al. 2000).

Furthermore, the unwieldy nature and high cost of traditional imaging methods is responsible for the lack of knowledge regarding cerebral hematoma growth. Few case studies are available which capture early cerebral hematoma growth (Fisher 2003), yet knowledge of early cerebral hematoma growth is limited by the lack of imaging data during the first hours after onset. The rate of growth of the hematoma during the first 4 hours are a determining factor in further hematoma expansion and mortality (Mayer 2003; Schlunk and Greenberg 2015).

## Aims

The objective of this thesis is to evaluate the ability of a monostatic radio-frequency resonator (RFR) in conjunction with deep learning models in detecting the rate change of volume.

The aims of this thesis are three-fold: 1) Create datasets of continuous  $S_{11}$  parameter measurements using an ex-vivo porcine model, 2) compare the performance of simple linear regression to that of several machine learning models such as logistic regression, random forest, and K-nearest neighbors in classifying flow rates from the generated datasets, 3) assess the feasibility of a CNN model in classifying flow rates from whole signal time-frequency images.

## References

- Brott, Thomas, Joseph Broderick, Rashmi Kothari, William Barsan, Thomas Tomsick, Laura Sauerbeck, Judith Spilker, John Duldner, and Jane Khoury. 1997. 'Early hemorrhage growth in patients with intracerebral hemorrhage', *Stroke*, 28: 1-5.
- Brouwers, H Bart, and Steven M Greenberg. 2013. 'Hematoma expansion following acute intracerebral hemorrhage', *Cerebrovascular diseases*, 35: 195-201.
- Edlow, Brian L, Riley M Bove, Anand Viswanathan, Steven M Greenberg, and Scott B Silverman. 2012. 'The pattern and pace of hyperacute hemorrhage expansion', *Neurocritical care*, 17: 250-54.
- Fisher, C Miller. 2003. 'Hypertensive cerebral hemorrhage. Demonstration of the source of bleeding', *Journal of Neuropathology & Experimental Neurology*, 62: 104-07.
- Liu, R, TJ Huynh, Y Huang, D Ramsay, K Hynynen, and RI Aviv. 2015. 'Modeling the pattern of contrast extravasation in acute intracerebral hemorrhage using dynamic contrast-enhanced MR', *Neurocritical care*, 22: 320-24.
- LoPresti, Melissa A, Samuel S Bruce, Elvis Camacho, Sudkir Kunchala, Byron G Dubois, Eliza Bruce, Geoff Appelboom, and E Sander Connolly Jr. 2014. 'Hematoma volume as the major determinant of outcomes after intracerebral hemorrhage', *Journal of the neurological sciences*, 345: 3-7.
- Magid-Bernstein, Jessica, Romuald Girard, Sean Polster, Abhinav Srinath, Sharbel Romanos, Issam A Awad, and Lauren H Sansing. 2022. 'Cerebral hemorrhage: pathophysiology, treatment, and future directions', *Circulation research*, 130: 1204-29.
- Marler, John R, BC Tilley, M Lu, Thomas G Brott, PC Lyden, JC Grotta, JP Broderick, SR Levine, MP Frankel, and SH Horowitz. 2000. 'Early stroke treatment associated with better outcome: the NINDS rt-PA stroke study', *Neurology*, 55: 1649-55.
- Mayer, Stephan A. 2003. 'Ultra-early hemostatic therapy for intracerebral hemorrhage', *Stroke*, 34: 224-29.

Patil, Smita, Rosanna Rossi, Duaa Jabrah, and Karen Doyle. 2022. 'Detection, diagnosis and treatment of Acute ischemic stroke: current and future perspectives', *Frontiers in medical technology*, 4: 748949.

Schlunk, Frieder, and Steven M Greenberg. 2015. 'The pathophysiology of intracerebral hemorrhage formation and expansion', *Translational stroke research*, 6: 257-63.

## CHAPTER II

### LITERATURE REVIEW

#### Background

The focus of this literature review will first be the pathophysiology of hemorrhagic stroke along with the current methods used in monitoring its development. This section is followed by a review of alternative monitoring methods which have been recently investigated. These methods include impedance, conductive, capacitive, and finally radio frequency sensing and imaging. The review will explore the theoretical underpinnings of these alternative methods and their advantages and disadvantages when compared to both traditional methods and to one another. The review will end with a table within which the methods and systems from a selection works which display key numerical, benchtop, and clinical studies investing these alternative methods.

#### Pathophysiology of Hemorrhagic stroke

##### *Early Understanding*

The first description of stroke was made by Hippocrates around 400 BC, coining the term Apoplexy (Garrison and McHenry 1969). Apoplexy, which translates to “struck down by violence”, was the preferred term for the affliction until 20<sup>th</sup> century (Pound, Bury, and Ebrahim 1997). Though at the time the leading theory for medicine considered an imbalance of the four humors (blood, phlegm, yellow bile, and black bile) to be the root cause of disease, Hippocrates still intuited the mechanism behind apoplexy to be a “stagnation or station of the Blood” (Allen 1829). This stagnation was once thought to be caused by an accumulation of black bile within the

brain. Considering this model of understanding, it is no surprise that bloodletting was the most common treatment for apoplexy at the time (Paciaroni and Bogousslavsky 2008).

In the 2<sup>nd</sup> century AD, Galen Pergamon theorized that the vasculature of the human brain contained a network of vessel called the rete mirabile or wonderful network. This theory was based on observations of pig and oxen cerebral vasculature, as the dissection and examination of the human body was considered to be taboo, limiting the progression of knowledge with regard to anatomy for hundreds of years (Tatu, Moulin, and Monnier 2005). Of course, there was no rete mirabile in the human brain, and the evidence to reject Galen's theory didn't come until the first accurate drawings of the human brain were made in Andrea Vesalius's *De humani corporis fabrica* published in 1543 (Vesalius 1543).

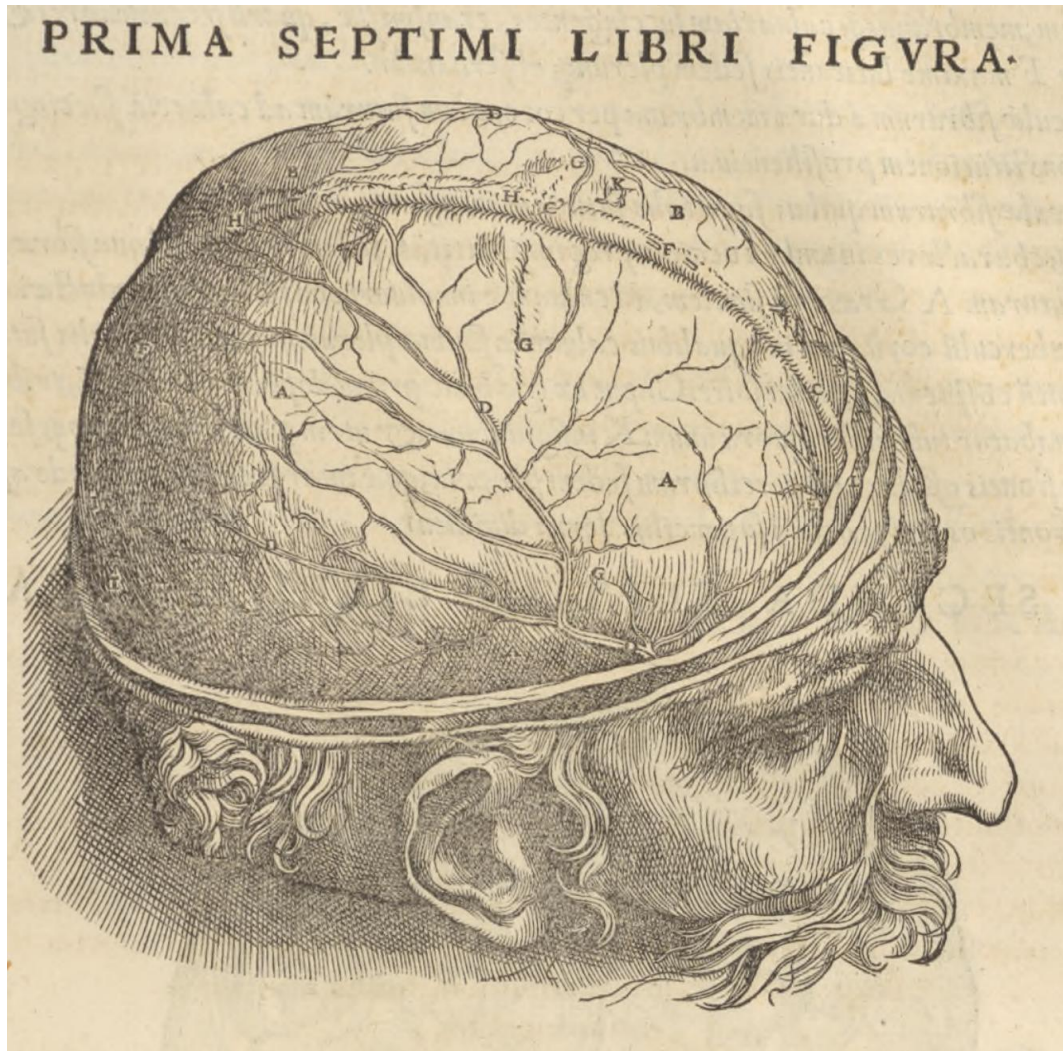


Figure 1: An illustration of the brain from Andrea Vesalus's *De humani corporis fabrica* (Vesalius 1543). Image Courtesy of the National Library of Medicine.

Stroke was not associated with bleeding in the brain until the 17<sup>th</sup> century when Johann Wepfer, a prolific contributor to the corpus of medical knowledge, examined stroke victims post-mortem. Wepfer would go on to officially denounce the *ret mirabile*, correlate lesions to the right side of the brain with speech disorders, and suggest that blockages in the brain could cause stroke (Gurdjian and Gurdjian 1979).

The 19<sup>th</sup> century saw several significant advances in the understanding of the mechanisms underlying stroke. Dr. Rudolph Virchow, the father of modern pathology, uncovered the

consequences of cutting off blood flow to organs, coining the term ischemia. Dr. Virchow also described clotting of the blood within the circulatory system, providing to the medical community yet more terminology which is still used to this day: thrombosis & Emboli (Schiller 1970).

A new concept akin to the modern understanding of the mechanism behind cerebral hemorrhage pathology was introduced by Carl Rokitansky. He suggested that the ossification of the arteries caused them to become brittle, and in conjunction with high blood pressure, could lead to hemorrhage (Paciaroni and Bogousslavsky 2008). In the mid-19<sup>th</sup> century, Jean-Martin Charcot and his associate Charles Bouchard, identified small expansion off of cerebral arteries called miliary aneurysms, now referred to as Charcot and Bouchard aneurysms, which may contribute to intracranial bleeding (Bouchard 1866).

### *Risk factors and mechanisms*

Hemorrhagic stroke remains a significant contributor to morbidity and mortality worldwide. Understanding the risk factors and mechanisms that lead to vessel rupture is essential for effective prevention and management strategies. Factors such as chronic hypertension, age, sex, cerebral amyloid angiopathy (CAA), and genetic predispositions increase susceptibility to hemorrhage. While considerable progress has been made in identifying these initial risk factors, less is known about the subsequent events following the initial rupture, particularly the mechanisms driving hematoma expansion. This section discusses the known risk factors and explores the underlying mechanisms contributing to hemorrhagic stroke.

Dr. Nicholas Robinson's "A discourse Upon the Nature and Cause of Sudden Deaths", published in 1732, offers insight into the intuited risk factors associated with stroke which predates

modern medical research, stating that “Those persons... (who) are in danger of sudden Death (from stroke)... are of an unwieldy, corpulent Body... have short Necks, strait Chests, and are subject to hitch in their Breathing; great, large Heads, with very sanguine or pale Countenance, if they indulge in a luxurious Manner of Living, seldom escape a sudden, fatal Stroke” (Robinson 1732).

Dr. Nicholas Robinson's descriptions can be equated to modern medical understanding by recognizing that an "unwieldy, corpulent body" refers to obesity, a significant risk factor for cardiovascular disease and stroke. The mention of "short necks" and "strait chests" suggests anatomical features that may contribute to respiratory issues such as sleep apnea, which is linked to increased cardiovascular risk. Individuals who "are subject to hitch in their breathing" likely experience breathing difficulties or chronic respiratory conditions. The observation of "great, large heads, with very sanguine or pale countenance" may indicate hypertension or circulatory problems affecting skin coloration. Lastly, indulging in a "luxurious manner of living" corresponds to a sedentary lifestyle with excessive consumption of rich foods and alcohol, leading to poor diet, lack of physical activity, and other unhealthy habits. Together, these factors are recognized today as significant contributors to the risk of stroke and sudden cardiac events (Morais Filho et al. 2021).



Figure 2: Portrait of Daniel Lambert (1770–1809), known for his exceptional corpulence. Artist: Unknown. Image courtesy of the Wellcome Collection. CC BY 4.0 (Unknown 1809)

Cerebral hemorrhage consists of two subtypes: Intracranial cerebral hemorrhage (ICH), which is the most common cerebral hemorrhage and is associated with a mortality rate of 70% in the first five years, and subarachnoid hemorrhage (SH), which is the leading cause of disability in

young patients suffer from stroke (Morais Filho et al. 2021). The two forms of hemorrhagic stroke differ in location, mechanism, and in underlying risk factors. ICH occurs in the parenchyma, or the functional substrate of the brain tissue, whereas SH occurs between the brain tissue and the most basal of the outer layers of the brain known as the arachnoid (Figure 3).

A single vessel weakened from chronic hypertension or atherosclerosis and usually forming an aneurysm, bursts causing the initial hematoma expansion. The pressure from this expansion causes injury, as pressure rises with the progression of the hematoma (Schlunk and Greenberg 2015). Since the human brain case is enclosed, pressure rises exponentially after the natural intracranial pressure compensatory system is exceeded. This causes herniation, inducing midline shift and condensing brain tissue below the site into the inferior confines of the cranium (Morais Filho et al. 2021).

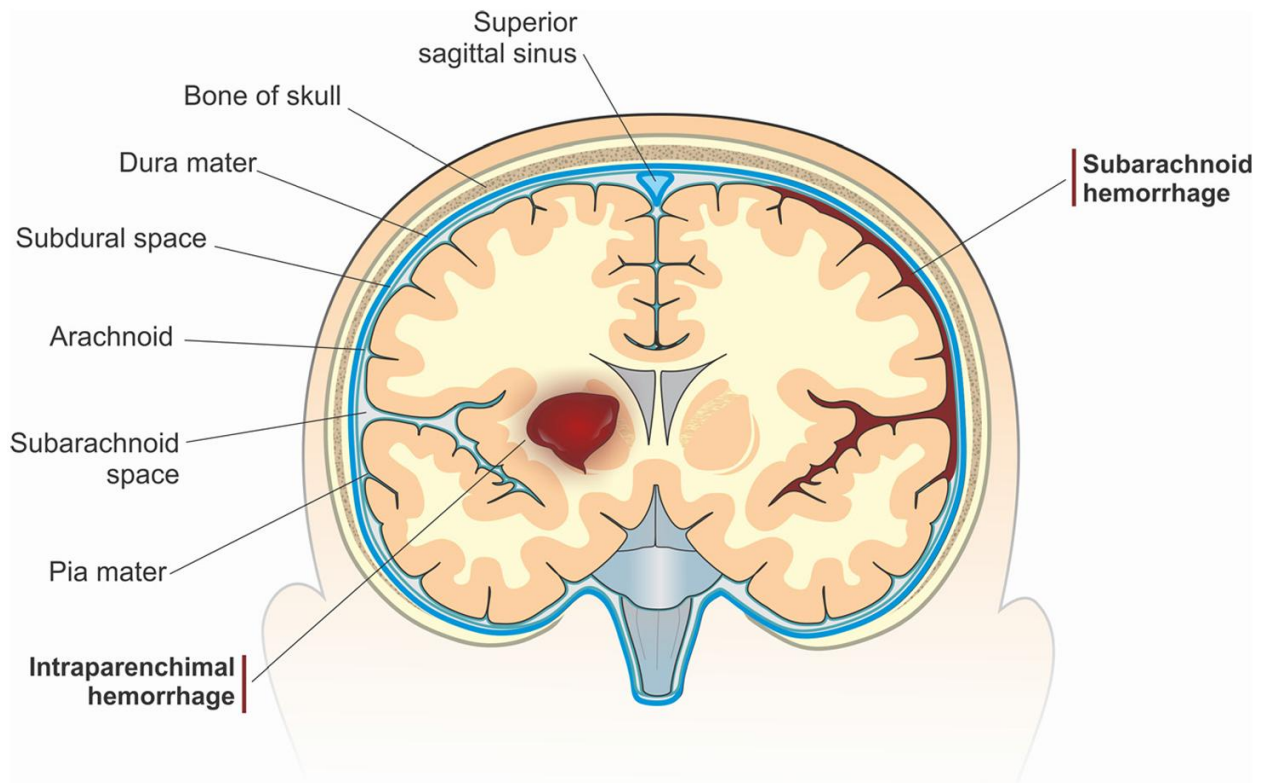


Figure 3: Comparison of location between ICH and SH, Courtesy of (Morais Filho, Rego et al. 2021)

The average age of those who suffer from SH is 55 years, and in 85% of the cases, the SH is caused by the rupturing of an intracranial aneurysm (Macdonald and Schweizer 2017). The mean age of ICH in a study with a cohort of 3,000 ethnically diverse patients found the mean age of onset to be 62.4 years (Woo et al. 2022). Small vessel disease (SVD), caused by both hypertension and CAA, are found to be the cause of ~80% of ICH. Hypertensive ICH presents itself in the deeper regions of the brain, whereas CAA tends more towards lobar incidents (Figure 4). The remaining 20% of cases are attributed to malformations of the cerebral vasculature and brain tumors (Mendiola et al. 2023).

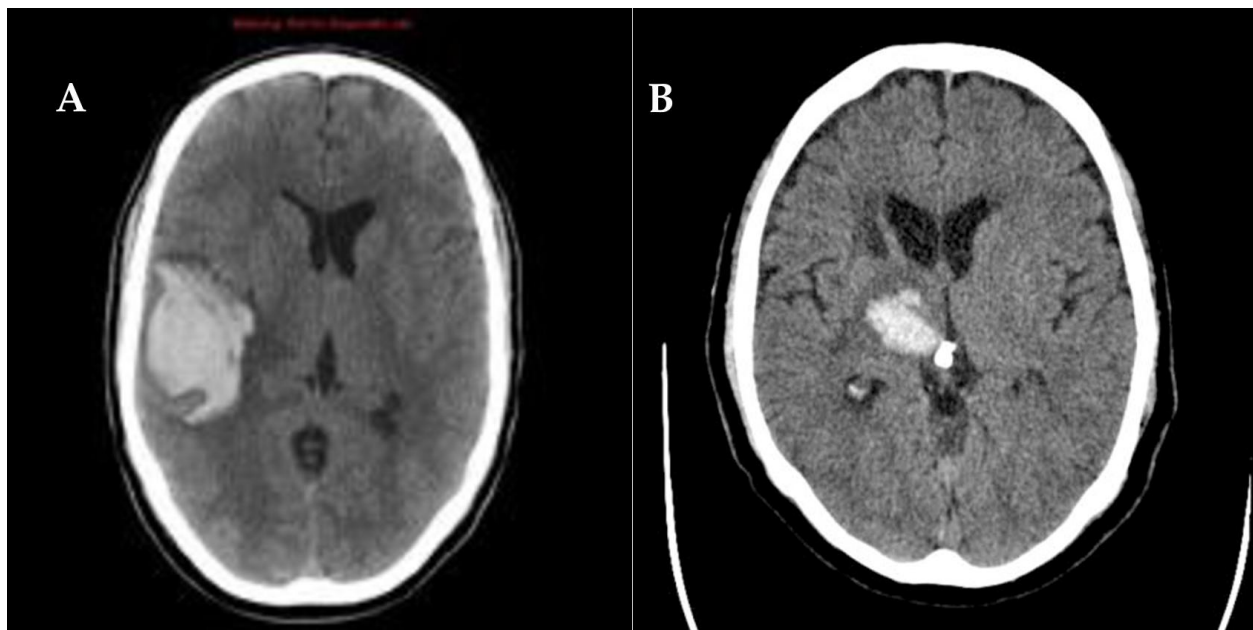


Figure 4: Comparison of lobar (A) vs deep (B) ICH, courtesy of (Mendiola, Arboix et al. 2023).

In some regions, as high as 25% of hemorrhagic stroke could be prevented by proper hypertension management (Woo et al. 2004). A meta-analysis of randomized control trials has found that a reduction of 10 mmHg in systolic blood pressure is associated with a 31% reduction in overall stroke risk (ischemic and hemorrhagic) (Lawes et al. 2004). The subpopulations affected

by, and mortality rates associated with, hemorrhagic stroke differ between those with amyloid angiopathy and chronic hypertension. For example, hypertension increases the risk of hematoma expansion after the initial bleed (Cappellari et al. 2015). The weakening of the lining of the cerebral vasculature, regardless of the driving factor, characterizes the pathophysiology of hemorrhagic stroke.

The smooth muscle cells (SMC) which are responsible for maintaining the structural integrity and contractibility of the vessels, dedifferentiate into an insecure, non-contractile and hyper-proliferative state (Starke et al. 2014). Hypertension causes smooth muscle cell dystrophy, atherosclerosis, and lipohyalinosis in the arterioles of the brain which eventually leads to an increase in pro-inflammatory biomarkers (Figure 5).

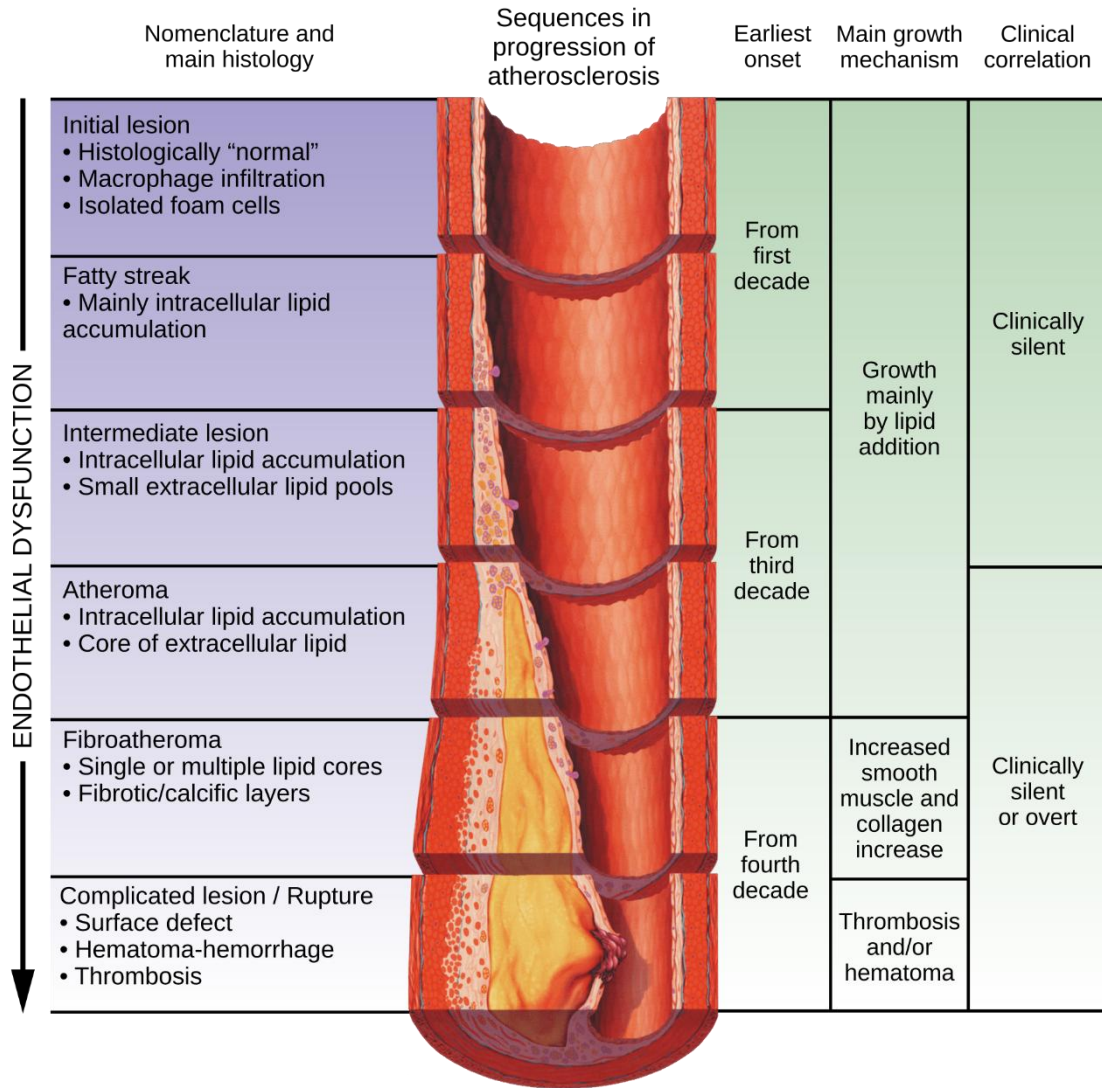


Figure 5: Progression of atherosclerosis. Courtesy of (YitzhakNat 2022).

The inflammation process triggers the destruction of the extracellular matrix surrounding the vessels by way of matrix metallo-proteinases (MMP). MMPs, released by macrophages, also cause apoptosis of the SMC which line the arterioles. Chalouhi et. al sums the inflammation process leading to aneurysm formation and rupture (Figure 6).

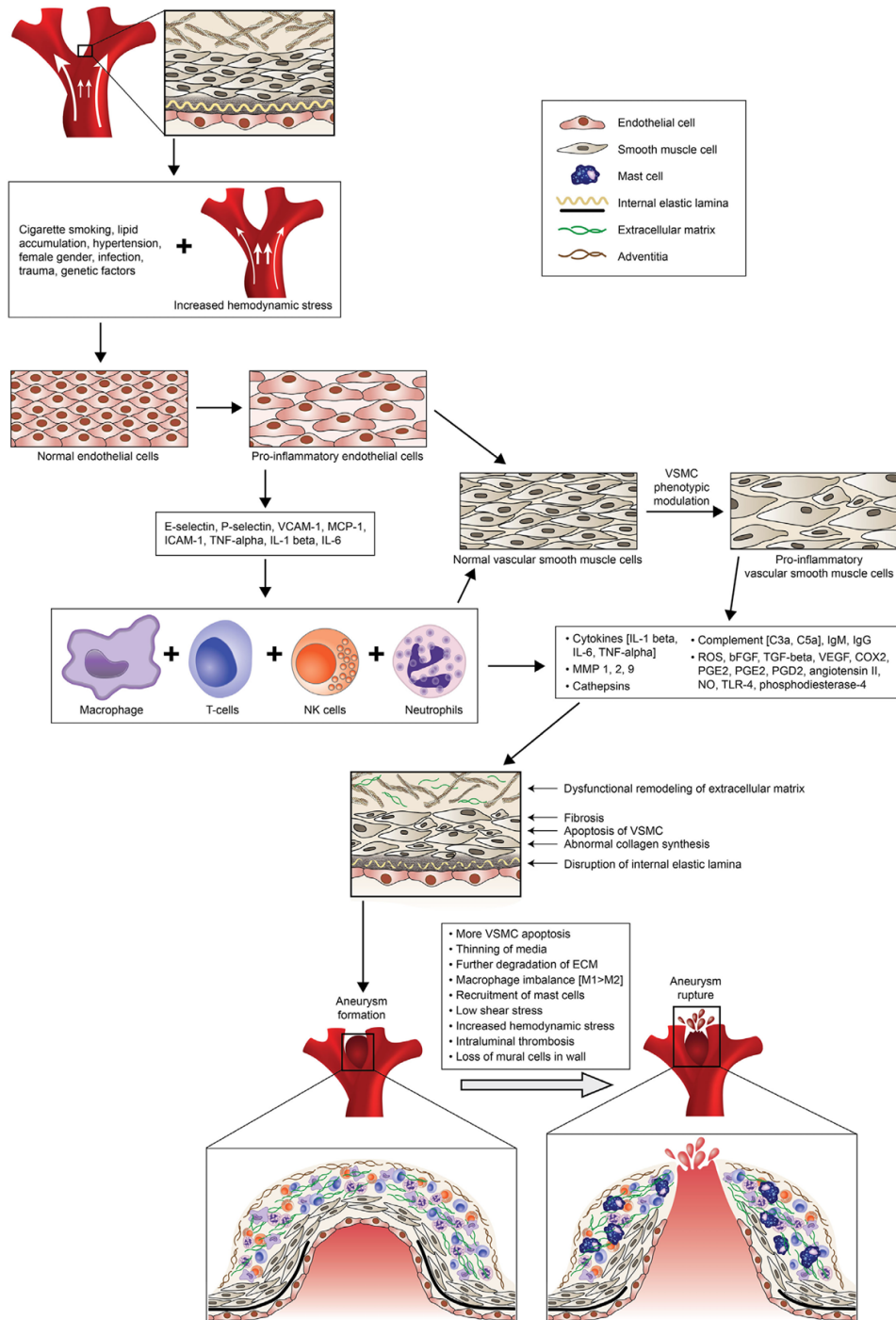


Figure 6: Risk factors such as smoking, atherosclerosis, hypertension and genetic predisposition contribute to inflammatory pathways which result in cerebral aneurysm formation and rupture. Courtesy of (Chalouhi, Hoh et al. 2013).

Populations which carry the apolipoprotein E2 or E4 (APOE2 & APOE4) alleles are at greater risk of developing ICH and experiencing recurrent bleeding (Martin et al. 2002). In fact, APOE2 and APOE4 genotypes experience recurrent bleed at four and two times the rate of APOE3 genotypes, respectively (Falcone and Woo 2017). Furthermore, APOE4 is associated with CAA which is found in ~70% of lobar ICH (Falcone and Woo 2017). This population not only experiences a higher rate of cognitive decline, but cerebral hemorrhage. Additionally, arterial hypertension, and the treatments which are typically used to treat it such as statins, further increase the risk of hemorrhagic stroke within this population (Block and Dafotakis 2017).

#### *Avalanche model of hematoma expansion*

Every 10% increase in hematoma volume increases the mortality rate by increasing by 5% (Brouwers and Greenberg 2013). An acute blood pressure spike may not only cause the initial hematoma but is associated with a greater chance of hematoma expansion (Morais Filho et al. 2021). The current understanding of hematoma formation and expansion, the avalanche model, was first proposed by Fisher in 1971 (Fisher 1971). The initial bleed expands rapidly at onset, its rate of growth being inversely proportional to the intracranial pressure. A base line volume will be reached and may be maintained for some time. Shear forces from the expansion causes adjacent vessels to rupture, causing secondary hematoma expansion (Figure 7). This cascading effect gives name to the avalanche model, and is seen in 11% of patients beyond 6 hours after onset (Brouwers and Greenberg 2013; Cappellari et al. 2015).

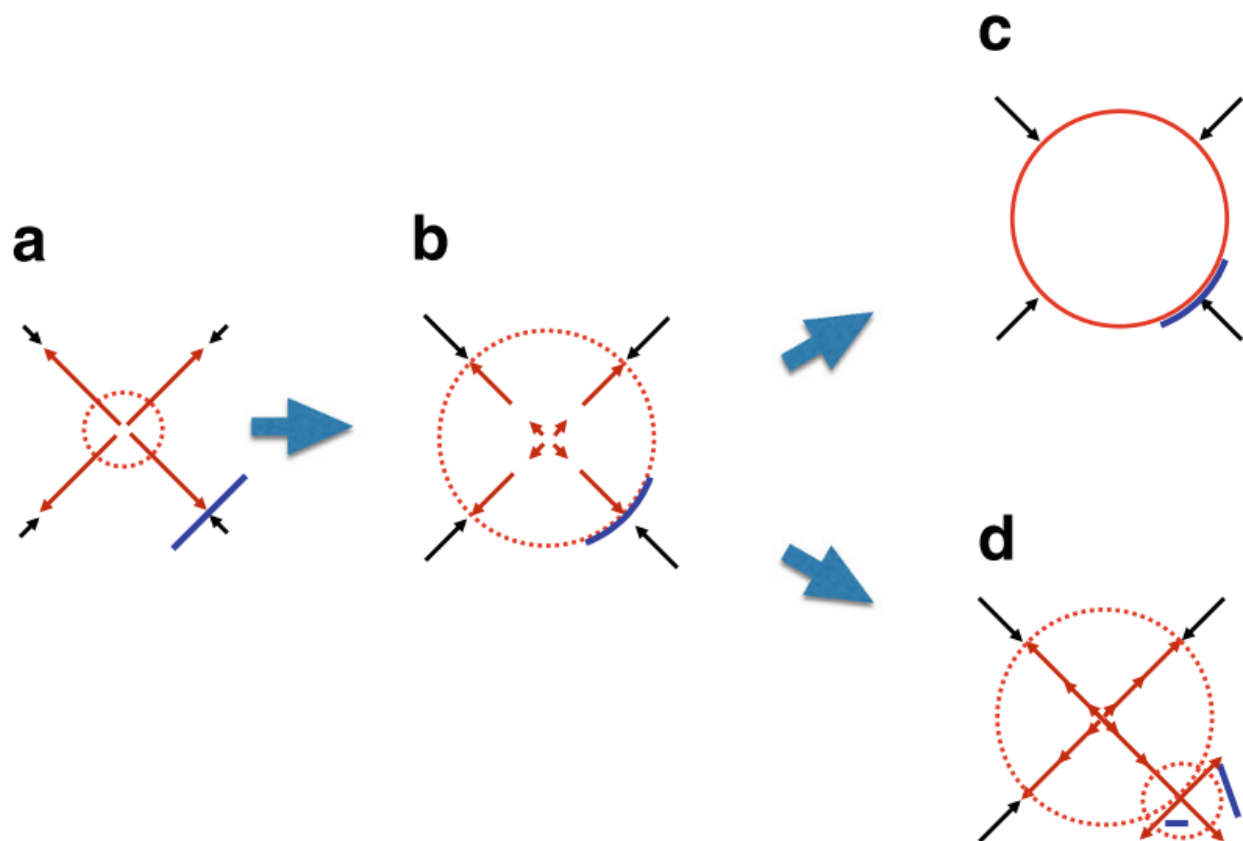


Figure 7: (a) Blood escapes from the initial rupture (red arrows), causing early hematoma formation (dashed circle) with minimal tissue counter-pressure (black arrows). (b) Hematoma growth increases pressure, stretching surrounding vessels (blue line). (c) Press

### *Current Monitoring Methods*

Currently, the primary methods for monitoring cerebral hemorrhage include computed tomography (CT), magnetic resonance imaging (MRI), and transcranial Doppler ultrasound (TCD). CT is often used due to its availability and speed; however, it has limitations in detecting smaller bleeds during the hyperacute phase. MRI provides high sensitivity for detecting microbleeds but is often impractical for emergency use due to time constraints and the need for patient stability (Patil et al. 2022; Manno 1997).

CT scans generally cost between \$500 and \$1,500 per scan, with additional costs for contrast materials if required. The time to complete a CT scan is typically 5-10 minutes, but this

can be extended due to patient preparation and waiting times (Smith-Bindman, Miglioretti, and Larson 2008). MRI scans are more expensive, ranging from \$1,000 to \$5,000, depending on the type of MRI and whether contrast is used. MRI procedures are also significantly longer, often taking 30-60 minutes per scan, with additional time for patient setup and stabilization (Smith-Bindman, Miglioretti, and Larson 2008). Furthermore, the average initial set up costs for stationary CT and MRI imaging systems were \$772,968 and \$1,689,568, respectively (Mohammadshahi et al. 2019). The high cost and longer duration make MRI less suitable for emergency situations compared to CT, despite its superior sensitivity in detecting small bleeds and microhemorrhages (Patil et al. 2022).

CT scans, while widely available and relatively inexpensive, have limited sensitivity in detecting small or early ischemic changes, especially in the posterior fossa. They also expose patients to ionizing radiation, which poses risks with repeated use. This exposure has been on the rise since the 90s, as examinations become longer and more frequent (Smith-Bindman, Miglioretti, and Larson 2008). MRI, on the other hand, has higher sensitivity for detecting early ischemia and microbleeds, but it is limited by higher costs, longer acquisition times, and contraindications in certain patients, such as those with metal implants or claustrophobia (Kidwell and Hsia 2006).

Dual-energy CT (DECT) and CT angiography (CTA) are recent advancements over conventional CT, providing improved diagnostic capabilities for detecting hemorrhagic and ischemic strokes. DECT allows better differentiation of hemorrhage from calcifications and has increased sensitivity in identifying smaller bleeds, while CTA provides detailed vascular imaging to identify vascular occlusions or aneurysms. However, these methods also have limitations. DECT is still limited by its reliance on ionizing radiation, and CTA requires the use of contrast agents,

which may be contraindicated in patients with kidney impairment or allergies (Christensen and Christensen 2018).

### Alternative Monitoring Methods

A number of alternative monitoring methods have been investigated in recent years with a focus on reducing cost, improving portability, and enhancing the ability to detect hemorrhage in its early stages. These methods include impedance-based monitoring, inductance, capacitance, and radio frequency (RF) sensing and imaging. Each method has unique theoretical underpinnings and practical applications.

#### *Impedance*

In 1932, Altzer and Lehmann conducted the first experiments capturing physiological changes via impedance plethysmography (Atzler and Lehmann 1932). Nyboer and Hannapel also made significant contributions to the understanding of electrical impedance in biological tissues, particularly in the context of plethysmography (Nyboer, Kreider, and Hannapel 1950). The first in vivo images using electrical impedance tomography were of the human forearm in 1982 using a 16 electrode array (Figure 8) (Brown and Barber 1982).

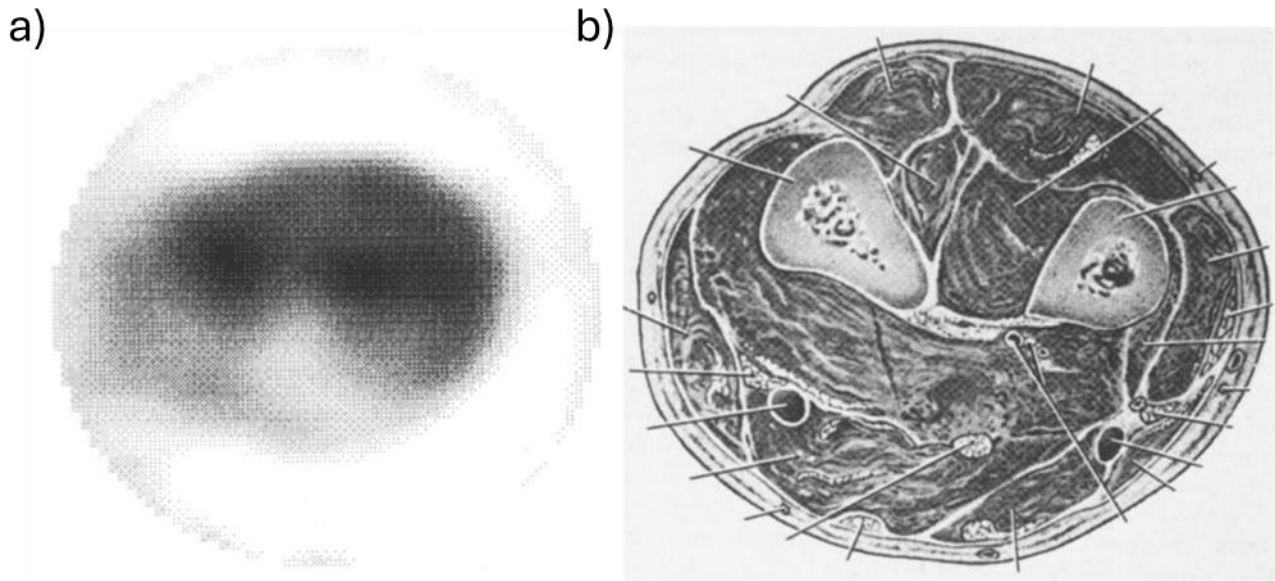


Figure 8: First image created via EIT (a) and a representative cross-section of a forearm (b), courtesy of (Brown and Barber 1982).

Electrical impedance has been used for cardiac stroke volume detection (Vonk-Noordegraaf et al. 2000), detection of ischemic stroke (Holder 1992; Dowrick, Blochet, and Holder 2015), functional lung imaging (Gong et al. 2015; Alruwaili et al. 2017),

The basic mechanism behind electrical impedance tomography is that an AC current or voltage signal applied by one or multiple transmitting electrodes while receiving electrodes measure the change in voltage around the field of interest (Figure 9)(Tiwari et al. 2023). The resistivity of tissue varies, and the dielectric properties of tissues are altered when in a diseased state; therefore, EIT is able to not only detect these changes, but differentiate between tissue types (Bera 2014; Ke et al. 2022).

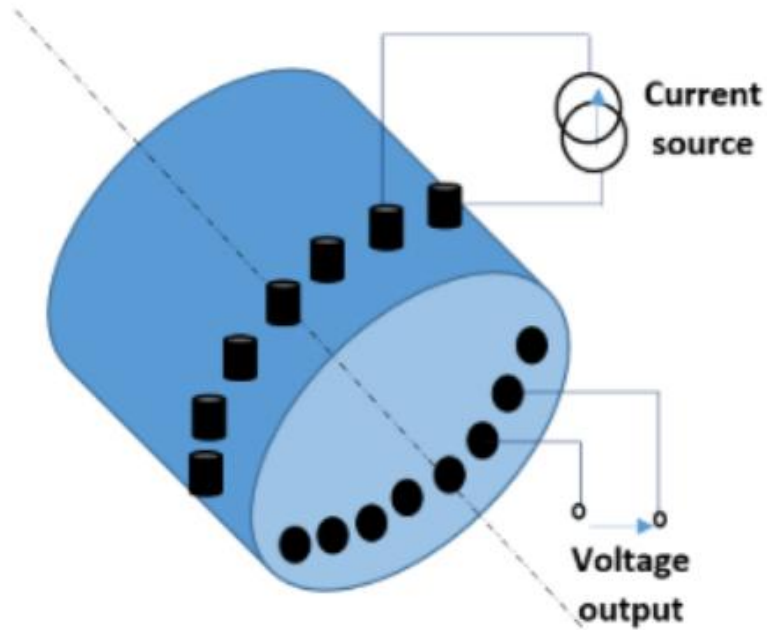


Figure 9: Electrodes are placed around the object of interest. A current source is applied to the transmitting electrodes, and the voltage output is measured at the receiving electrodes. Courtesy of (Tiwari, Meribout et al. 2023).

The forward problem, represented by Equation 1, is used to predict the electrical potential distribution of an imaging field by known conductivity distribution and excitation current:

$$\nabla(\sigma(x)\nabla\phi(x)) = 0, \quad x \in \Omega$$

Equation 1

Where  $\sigma(x)$  is the distribution of conductivity and  $\phi(x)$  is the electrical potential in the measured field. By solving this equation, current changes in current along within the domain is given. The boundary conditions are described in Equation 2:

$$\left\{ \sigma(x) * \frac{\partial \phi(x)}{\partial n} = 0, x \in \partial \Omega \cup_{\{l=1\}}^L e_l \right.$$

$$\left. \left\{ u(x) + z_l \sigma(x) * \frac{\partial \phi(x)}{\partial n} = \psi_l, x \in e_l \right. \right.$$

$$\left. \left\{ \int_{e_l} \sigma(x) * \frac{\partial \phi(x)}{\partial n} dS = I_l \right. \right.$$

Equation 2

Where  $z_l$ ,  $I_l$ ,  $\psi_l$ , and  $L$  are the electrode, contact impedance, injected current and electrical potential, and number of electrodes respectively. Due to the complexity of the boundary conditions, a finite element method is used to approximate a solution to the problem. However, this is computationally intensive (Shi, Tian, and Wang 2021).

Recent studies have demonstrated the effectiveness of impedance-based imaging techniques for detecting and monitoring ICH and other cerebrovascular conditions. (Shi, Tian, and Wang 2021) conducted a numerical study to explore the simultaneous reconstruction of hemorrhage and ischemia using EIT. Their work showcased the potential of superimposed imaging methods to improve image quality, though challenges such as the ill-posed nature of the inverse problem persisted. (Dowrick, Blochet, and Holder 2015) took a different approach by performing bioimpedance measurements in rat models during stroke and epilepsy events. Their findings highlighted conductivity changes that correlated with stroke and seizure activities, suggesting the potential utility of EIT as a tool for real-time monitoring of brain activity. (Wang et al. 2016) further validated the applicability of EIT by employing it in a benchtop model of head phantoms for ICH detection. The study revealed that impedance changes were sensitive to the injected blood, illustrating the viability of EIT for early diagnosis of ICH in various scenarios.

In the context of animal models, (Murphy et al. 2022) applied electrical impedance measurements to detect subclinical hemorrhage in a porcine model. Their study demonstrated the superior early detection capabilities of impedance-based monitoring compared to standard clinical metrics, achieving a high accuracy without the need for imaging reconstructions. Similarly, (Park et al. 2024) utilized bioelectrical impedance analysis in a swine model to evaluate hemodynamic and impedance changes during hypovolemic shock. The study found that impedance analysis effectively correlated with changes in stroke volume (SV) and mean arterial pressure (MAP), and that a balanced crystalloid with 20% albumin was most effective in restoring hemodynamic parameters. While there are promising results in both experimental and animal models, further validation and optimization are necessary to enhance clinical translation and real-world applicability.

The major limitations for impedance based monitoring methods are three-fold: 1) interfering impedance from skin-electrode contact and the skull, 2) limited model accuracy due to heterogeneity of the head, and 3) computational intensity of the reconstruction algorithms (Ke et al. 2022)

### *Inductance*

The basic principle of magnetic inductance tomography (MIT) is that an alternating magnetic field  $B_0$ , induces currents within an object which are orthogonal to  $B_0$ . These eddy currents then produce a smaller magnetic field,  $\theta B$ , which alters  $B_0$ , creating an encompassing field,  $B_T$ :

$$B_T = B_0 + \theta B$$

Equation 3

The phase shift,  $\theta\psi$ , is calculate by taking the dot product between  $B_0$  and  $B_T$  divided by their magnitudes multiplied (Equation 4):

$$\cos \theta\psi = \frac{B_0 \cdot B_T}{|B_0||B_T|}$$

Equation 4

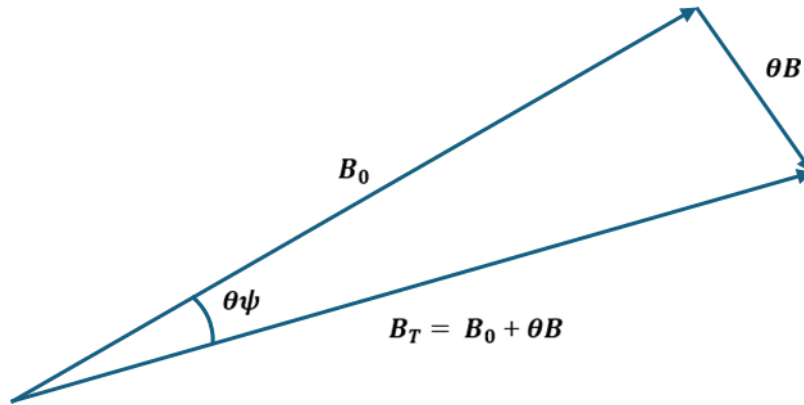


Figure 10: Vector representation of the relationship between the initial magnetic field  $B_0$ , the induced field  $\theta B$ , the resultant magnetic field  $B_T$ , and the phase shift  $\theta\psi$ .

MIT reconstructs images by measuring the phase shift,  $\theta\psi$ , caused by the field,  $\theta B$ , induced by the eddy currents. In the case of biological tissue, this shift is very small, as the conductivity of tissue is relatively small. In order to solve the inverse problem to reconstruct the dielectric properties of the imaged object, the forward vector function (Equation 1) is used within the context of the influence of the material's magnetic permeability on the resulting electromagnetic field distribution.

Oziel, Korenstein, and Rubinsky (2018) conducted numerical studies using a single inductive coil, demonstrating the potential for non-contact monitoring of temporal volume changes in a hematoma. A subsequent study by Oziel, Rubinsky, and Korenstein (2020) employed a benchtop PVC head phantom using calf brain tissue, comparing free injections of blood to balloon-induced injections. Wang (2018) explored the use of a 16-element inductive array in a numerical study, highlighting the promise of multi-element systems for enhanced spatial resolution.

Recent studies have utilized inductance-based methods and near-field coupling for ICH and stroke detection, highlighting different approaches and their effectiveness. (Oziel, Korenstein, and Rubinsky 2018) conducted a numerical study using an inductive coil to monitor changes in hematoma volume in a human head model. Their findings showed that the inductive coil was sensitive to volume changes, although the accuracy required multi-frequency measurements. Building on this, (Oziel, Rubinsky, and Korenstein 2020) employed an inductive coil to measure the scattering parameters ( $S_{21}$ ) in a human skull model, successfully detecting changes in tissue-to-fluid ratios with high accuracy, although noise and artifacts presented challenges. (Bai et al. 2019) also demonstrated the potential of inductance-based detection by employing a single excitation coil and a receiving coil to measure permittivity changes in rabbit heads, indicating feasibility for detecting intracranial hemorrhage through significant declines in real part measurements during blood injection. Similarly, (Chen, Tan, and Dong 2020) analyzed excitation strategies for Magnetic Induction Tomography (MIT) to enhance sensitivity and accuracy in detecting ICH, using numerical simulations to identify optimal configurations, which underscores the importance of refined excitation techniques in inductance-based imaging.

Near-field coupling has also been investigated for its potential to assess cerebrovascular conditions. (Li et al. 2022) employed a multi-parameter near-field coupling (NFC) sensing system for the early assessment of acute ischemic stroke (AIS) in rabbit models. By measuring phase and amplitude changes, they were able to achieve high classification accuracy for AIS monitoring using a backpropagation (BP) network. Although environmental interference affected measurements and the study was limited to animal models, the promising results indicate the potential of NFC in dynamic cerebrovascular monitoring.

The major limitation with inductive imaging such as MIT, is that the magnetic field induced by the eddy currents is extremely small and hard to detect and the conductivity of blood is not very distinct from other tissues. A potential solution to this problem has been the recent investigation into capacitive imaging modalities (Xu et al. 2023).

### *Capacitance*

Capacitance imaging, also known as Electrical Capacitance Tomography (ECT), is an imaging technique similar in principle to Magnetic Inductance Tomography (MIT), but instead of focusing on magnetic induction, it measures capacitance changes within the imaged object. ECT utilizes multiple electrodes placed around the object to sense changes in permittivity, which is directly related to the dielectric properties of the medium. By measuring capacitance, ECT allows for more sensitive detection of small changes in tissue composition compared to MIT.

Some of the earlier use of capacitance for measuring changes in the physiological state of tissues was by (Hyman, Burnap, and Figar 1963; Hyman et al. 1964). Similar to the early work on impedance-based technology, Hyman's work focused on measuring blood flow via a capacitive plethysmography cuff.

Blood has a much higher permittivity (approximately 3000) compared to grey matter (990) and cerebrospinal fluid (CSF) (108). This significant contrast allows for the detection of hemorrhage based on changes in capacitance (Gabriel, Lau, and Gabriel 1996). By using capacitance instead of simply focusing on magnetic properties like permeability, capacitance imaging provides a more direct measurement of dielectric changes. This makes it a powerful tool for detecting and imaging intracerebral hemorrhages (ICH), offering a higher sensitivity to changes in tissue properties than traditional MIT.

Recent studies have investigated the use of capacitance-based imaging for detecting intracerebral hemorrhage (ICH). (Xu et al. 2023) conducted a pilot study on intracerebral hemorrhage imaging using Electrical Capacitance Tomography (ECT) with a 16-electrode system. Their study utilized both numerical simulations and ex vivo porcine brain models, demonstrating successful imaging of bleeding areas, although with some positional inaccuracies. (Huang et al. 2024) further investigated ECT for ICH detection, employing a symmetrical cancellation method across numerical, benchtop, and animal models. Their results suggested promising potential for prehospital emergency applications, but imaging accuracy was highly dependent on symmetrical alignment, with mirrored artifacts observed due to the cancellation approach.

(Peng et al. 2023) introduced a novel capacitance-based approach for ICH detection through frequency-dependent variations in permittivity. (Che et al. 2023) developed an eight-electrode ECT system for noninvasive, real-time detection of flowing thrombus, conducting dynamic experiments with fresh porcine blood clots. This study demonstrated the feasibility of using ECT for thrombus detection, highlighting its potential for real-time imaging, though further optimization for anti-interference capabilities is needed. (Bai et al. 2021) also contributed by using a parallel-plate capacitor to detect hemorrhage in rabbit models, demonstrating that capacitance

increased proportionally with the volume of blood injected, indicating its feasibility for non-invasive hemorrhage detection.

### *Radio Frequency (RF)*

Jacques Arsène d'Arsonval was a pioneering French physician whose work laid the foundation for radio frequency (RF) imaging. He was among the first to demonstrate the effects of high-frequency alternating current on biological tissue, showing that these currents could pass through the body safely and produce therapeutic effects without discomfort. This work provided the groundwork for understanding electromagnetic fields' interactions with biological tissues, a key concept in RF imaging today (d'Arsonval 1891).

Radio frequency imaging relies on the interaction between electromagnetic waves and biological tissues to generate diagnostic images. When RF waves are transmitted into the body, they induce electric currents in tissues. The response of the tissues varies depending on their composition and health. By analyzing how different tissues attenuate, reflect, or transmit these waves, RF imaging systems can create contrast images that highlight abnormalities. This technique is particularly useful in detecting issues such as hemorrhages or tumors, where the dielectric properties of affected tissues differ significantly from those of healthy tissues, allowing for non-invasive and real-time diagnostics.

Recent advances in radio frequency (RF)-based imaging have shown promise in detecting and differentiating cerebrovascular events such as hemorrhagic and ischemic strokes. (Alon and Dehkharghani 2021) developed a framework for stroke detection using broadband microwave scattering combined with deep learning on stochastic models. Their numerical study achieved over 94% accuracy in detecting hemorrhagic strokes, highlighting the potential of deep neural networks

(DNNs) in effectively interpreting dielectric properties associated with hemorrhages. Similarly, (Rodriguez-Duarte et al. 2021) validated the use of a microwave imaging system for 3D brain stroke imaging. Using a head phantom and ex vivo calf brains, they successfully localized both hemorrhagic and ischemic strokes, demonstrating the capabilities of microwave-based approaches for stroke detection, although the resolution remained lower than conventional imaging techniques.

(Tal and Shapira 2019) also investigated early diagnosis of stroke and internal hemorrhage using a combination of microwave sensing and deep neural network inference, achieving a sensitivity of 92.9% for hemorrhage detection. Their work demonstrated the feasibility of a compact, autonomous system suitable for out-of-hospital use. Further research has explored the utility of RF-based imaging for in vivo models. Further research has explored the utility of RF-based imaging for in vivo models. (Wang et al. 2020) investigated the differential diagnosis of hemorrhagic and ischemic strokes in rabbits using microwave scattering measurements. Their study demonstrated high accuracy rates in distinguishing hemorrhagic (93.75%) and ischemic (91.7%) strokes, supporting the feasibility of a portable and non-invasive diagnostic system for prehospital settings. (Zhang et al. 2019) also examined RF-based detection of cerebral hemorrhage using broadband antennas on rabbits. They observed that phase difference changes correlated with increasing bleeding volumes, indicating the promise of non-contact monitoring methods for intracranial hemorrhage. These studies collectively highlight the effectiveness of RF-based imaging for stroke and hemorrhage detection, showcasing the potential for non-invasive, portable diagnostic systems suitable for emergency and prehospital environments, though limitations in resolution and sensitivity remain areas for further development.

## References

- Allen, Benjamin. 1829. *The Natural History of the Chalybeat and Purging Waters of England with Their Particular Essays and Uses. Among which are Treated at Large the Apoplexy & Hypochondriacism... By Benjamin Allen Med. Bac* (and sold by S. Smith and B. Walford).
- Alon, Leeor, and Seena Dehkharghani. 2021. 'A stroke detection and discrimination framework using broadband microwave scattering on stochastic models with deep learning', *Scientific reports*, 11: 24222.
- Alruwaili, Fayez H, Jacob Griffith, Kim Cluff, and Jeremy Patterson. 2017. 'Non-invasive point-of-care method for measuring left-ventricular stroke-volume using a passive electromagnetic skin patch sensor', *Journal of the American College of Cardiology*, 69: 1068.
- Atzler, Edgar, and Gunther Lehmann. 1932. 'Über ein neues verfahren zur darstellung der herztätigkeit (Dielektrographie)', *Arbeitsphysiologie*, 5: 636-80.
- Bai, Zelin, Haocheng Li, Jingbo Chen, Wei Zhuang, Gen Li, Mingsheng Chen, Jia Xu, Shuanglin Zhao, Yuening Liu, and Jian Sun. 2021. 'Research on the measurement of intracranial hemorrhage in rabbits by a parallel-plate capacitor', *PeerJ*, 9: e10583.
- Bai, Zelin, Qingguang Yan, Gen Li, Wei Zhuang, Jingbo Chen, Jun Yang, Jia Xu, Lin Lu, Mingsheng Chen, and Lin Xu. 2019. 'Detection of rabbit intracranial hemorrhage based on permittivity', *Measurement Science and Technology*, 30: 115701.
- Bera, Tushar Kanti. 2014. 'Bioelectrical impedance methods for noninvasive health monitoring: a review', *Journal of medical engineering*, 2014: 381251.
- Block, Frank, and Manuel Dafotakis. 2017. 'Cerebral amyloid angiopathy in stroke medicine', *Deutsches Ärzteblatt International*, 114: 37.
- Bouchard, C Jacques. 1866. 'Etude sur quelques points de la pathogénie des hémorragies cérébrales.(Cand. Charles-Jacques Bouchard)'.

- Brouwers, H Bart, and Steven M Greenberg. 2013. 'Hematoma expansion following acute intracerebral hemorrhage', *Cerebrovascular diseases*, 35: 195-201.
- Brown, BH, and DC Barber. 1982. "Applied potential tomography-A new in vivo medical imaging technique." In *Proc Hosp Phys Annu Conf Sheffield Clin Phys Physiol Meas*.
- Cappellari, Manuel, Cecilia Zivelonghi, Giuseppe Moretto, Nicola Micheletti, Monica Carletti, Giampaolo Tomelleri, and Paolo Bovi. 2015. 'The etiologic subtype of intracerebral hemorrhage may influence the risk of significant hematoma expansion', *Journal of the neurological sciences*, 359: 293-97.
- Che, Quanqi, Hao Wang, Zhiwei Li, Hongtao Wu, Bai Chen, Kai Liu, and Jiafeng Yao. 2023. 'Noninvasive Image Reconstruction of Flowing Thrombus With Electrical Capacitance Tomography', *IEEE Sensors Journal*, 23: 5949-55.
- Chen, Yixuan, Chao Tan, and Feng Dong. 2020. "Excitation Strategy Analysis of Magnetic Induction Tomography for Intracranial Hemorrhage Detection." In *2020 39th Chinese Control Conference (CCC)*, 2780-85. IEEE.
- Christensen, Anders Fogh, and Hanne Christensen. 2018. 'imaging in acute Stroke—New options and State of the art', *Frontiers in Neurology*, 8: 736.
- d'Arsonval, MA. 1891. 'Action physiologique des courants alternatifs', *CR Soc Biol*, 43: 283-86.
- Dowrick, T, C Blochet, and D Holder. 2015. 'In vivo bioimpedance measurement of healthy and ischaemic rat brain: implications for stroke imaging using electrical impedance tomography', *Physiological measurement*, 36: 1273-82.
- Falcone, Guido J, and Daniel Woo. 2017. 'Genetics of spontaneous intracerebral hemorrhage', *Stroke*, 48: 3420-24.
- Fisher, C Miller. 1971. 'Pathological observations in hypertensive cerebral hemorrhage', *Journal of Neuropathology & Experimental Neurology*, 30: 536-50.
- Gabriel, Sami, RW Lau, and Camelia Gabriel. 1996. 'The dielectric properties of biological tissues: II. Measurements in the frequency range 10 Hz to 20 GHz', *Physics in medicine & biology*, 41: 2251.

- Garrison, Fielding Hudson, and Lawrence C McHenry. 1969. 'Garrison's History of neurology', *(No Title)*.
- Gong, Bo, Sabine Krueger-Ziolek, Knut Moeller, Benjamin Schullcke, and Zhanqi Zhao. 2015. 'Electrical impedance tomography: functional lung imaging on its way to clinical practice?', *Expert review of respiratory medicine*, 9: 721-37.
- Gurdjian, E Steven, and Edwin S Gurdjian. 1979. 'History of occlusive cerebrovascular disease: I. From Wepfer to Moniz', *Archives of neurology*, 36: 340-43.
- Holder, DS. 1992. 'Detection of cerebral ischaemia in the anaesthetised rat by impedance measurement with scalp electrodes: implications for non-invasive imaging of stroke by electrical impedance tomography', *Clinical Physics and Physiological Measurement*, 13: 63.
- Huang, Jing, Feng Chen, Ke Wang, and Sheng Chen. 2024. 'Research on electrical capacitance tomography (ECT) detection of cerebral hemorrhage based on symmetrical cancellation method', *Frontiers in Physics*, 12: 1392767.
- Hyman, Chester, Donald Burnap, and Štěpán Figar. 1963. 'Bilateral differences in forearm blood flow as measured with capacitance plethysmograph', *Journal of Applied Physiology*, 18: 997-1002.
- Hyman, Chester, Terry Greeson, Milton Clem, and David Winsor. 1964. 'Capacitance-plethysmograph method for separating blood flow in muscle and skin in the human forearm', *American Heart Journal*, 68: 508-14.
- Ke, Xi-Yang, Wei Hou, Qi Huang, Xue Hou, Xue-Ying Bao, Wei-Xuan Kong, Cheng-Xiang Li, Yu-Qi Qiu, Si-Yi Hu, and Li-Hua Dong. 2022. 'Advances in electrical impedance tomography-based brain imaging', *Military Medical Research*, 9: 10.
- Kidwell, Chelsea S, and Amie W Hsia. 2006. 'Imaging of the brain and cerebral vasculature in patients with suspected stroke: advantages and disadvantages of CT and MRI', *Current neurology and neuroscience reports*, 6: 9-16.
- Lawes, Carlene MM, Derrick A Bennett, Valery L Feigin, and Anthony Rodgers. 2004. 'Blood pressure and stroke: an overview of published reviews', *Stroke*, 35: 776-85.

- Li, Gen, Shengtong Yin, Man Jian, Jingbo Chen, Lingxi Zeng, Zelin Bai, Wei Zhuang, Bingxin Xu, Shengjie He, and Jian Sun. 2022. 'Early assessment of acute ischemic stroke in rabbits based on multi-parameter near-field coupling sensing', *BioMedical Engineering OnLine*, 21: 1-19.
- Macdonald, R Loch, and Tom A Schweizer. 2017. 'Spontaneous subarachnoid haemorrhage', *The Lancet*, 389: 655-66.
- Manno, Edward M. 1997. 'Transcranial Doppler ultrasonography in the neurocritical care unit', *Critical care clinics*, 13: 79-104.
- Martin, David S., Donna A. South, Margie L. Wood, Michael W. Bungo, and Janice V. Meck. 2002. 'Comparison of echocardiographic changes after short- and long-duration spaceflight', *Aviation, space, and environmental medicine*, 73: 532-36.
- Mendiola, Joana Maria Flaquer-Pérez de, Adrià Arboix, Luís García-Eroles, and Maria José Sánchez-López. 2023. 'Acute Spontaneous Lobar Cerebral Hemorrhages Present a Different Clinical Profile and a More Severe Early Prognosis than Deep Subcortical Intracerebral Hemorrhages—A Hospital-Based Stroke Registry Study', *Biomedicines*, 11: 223.
- Mohammadshahi, Marita, Minoo Alipouri Sakha, Atefeh Esfandiari, Maryam Shirvani, and Ali Akbari Sari. 2019. 'Cost effectiveness of mobile versus fixed computed tomography and magnetic resonance imaging: a systematic review', *Iranian Journal of Public Health*, 48: 1418.
- Morais Filho, A. B., T. L. H. Rego, L. L. Mendonca, S. S. Almeida, M. L. D. Nobrega, T. O. Palmieri, G. Z. D. Giustina, J. P. Melo, F. I. Pinheiro, and F. P. Guzen. 2021. 'The physiopathology of spontaneous hemorrhagic stroke: a systematic review', *Rev Neurosci*, 32: 631-58.
- Murphy, Ethan K, Samuel B Klein, Alexandra Hamlin, Justin E Anderson, Joseph M Minichiello, Alexander L Lindqwister, Karen L Moodie, Zachary J Wanken, Jackson T Read, and Victor A Borza. 2022. 'Detection of subclinical hemorrhage using electrical impedance: a porcine study', *Physiological measurement*, 43: 055001.
- Nyboer, Jan, Marian M Kreider, and Leonard Hannapel. 1950. 'Electrical impedance plethysmography: A physical and physiologic approach to peripheral vascular study', *Circulation*, 2: 811-21.

- Oziel, Moshe, Rafi Korenstein, and Boris Rubinsky. 2018. 'Non-contact monitoring of temporal volume changes of a hematoma in the head by a single inductive coil: a numerical study', *IEEE Transactions on Biomedical Engineering*, 66: 1328-36.
- Oziel, Moshe, Boris Rubinsky, and Rafi Korenstein. 2020. 'Detection and estimating the blood accumulation volume of brain hemorrhage in a human anatomical skull using a RF single coil', *PeerJ*, 8: e10416.
- Paciaroni, Maurizio, and Julien Bogousslavsky. 2008. 'The history of stroke and cerebrovascular disease', *Handbook of clinical neurology*, 92: 3-28.
- Park, Hoonsung, Hanyoung Lee, Seungmin Baik, and Jae-Myeong Lee. 2024. 'Analysis of hemodynamics and impedance using bioelectrical impedance analysis in hypovolemic shock-induced swine model', *Scientific reports*, 14: 15077.
- Patil, Smita, Rosanna Rossi, Duaa Jabrah, and Karen Doyle. 2022. 'Detection, diagnosis and treatment of Acute ischemic stroke: current and future perspectives', *Frontiers in medical technology*, 4: 748949.
- Peng, Shixin, Xiaoshu Wang, Gui Jin, Feng Wang, Ji Zhu, Xiaodong Zhang, Nan Liu, and Rui Xu. 2023. 'Study on detection of intracerebral hemorrhage based on frequency difference of permittivity', *Frontiers in Physics*, 11: 1333185.
- Pound, Pandora, Michael Bury, and Shah Ebrahim. 1997. 'From apoplexy to stroke', *Age and ageing*, 26: 331-37.
- Robinson, Nicholas. 1732. *A Discourse Upon the Nature and Cause of Sudden Deaths: And the Reason why Such Numbers of People Died Suddenly in the Years 1730 and 1731; with the Most Proper Indications Both to Discover the Danger, and Prevent the Fatal Stroke from Taking Effect. To which is Added, A Dissertation Upon Bleeding in a Fit of the Apoplexy; with Remarks Upon the Case of an Illustrious Person that Lately Dy'd Abroad Upon His Travels. To which is Prefix'd. A Preface in Defence of the Theory of Medicine, Against the Cavils and Exceptions of Some Late Writers: Clearly Demonstration, that Hippocrates, Galen, and All the Great Ancients Grounded Their Practical Indications Upon Principles, and a Theory. By Nicholas Robinson, MD And a Member of the College of Physicians, London* (T. Warner, at the Black-Boy, in Pater-Noster-Row).
- Rodriguez-Duarte, David O, Jorge A Tobon Vasquez, Rosa Scapatucci, Giovanna Turvani, Marta Cavagnaro, Mario R Casu, Lorenzo Crocco, and Francesca Vipiana. 2021. 'Experimental validation of a microwave system for brain stroke 3-d imaging', *Diagnostics*, 11: 1232.

- Schiller, Francis. 1970. 'Concepts of stroke before and after Virchow', *Medical history*, 14: 115-31.
- Schlunk, Frieder, and Steven M Greenberg. 2015. 'The pathophysiology of intracerebral hemorrhage formation and expansion', *Translational stroke research*, 6: 257-63.
- Shi, Yanyan, Zhiwei Tian, and Meng Wang. 2021. "Simultaneous Imaging of Intracerebral Hemorrhage and Secondary Ischemia with Electrical Impedance Tomography." In *2021 IEEE International Conference on Consumer Electronics and Computer Engineering (ICCECE)*, 723-26. IEEE.
- Smith-Bindman, Rebecca, Diana L Miglioretti, and Eric B Larson. 2008. 'Rising use of diagnostic medical imaging in a large integrated health system', *Health affairs*, 27: 1491-502.
- Starke, Robert M, Nohra Chalouhi, Dale Ding, Daniel MS Raper, M Sean Mckisic, Gary K Owens, David M Hasan, Ricky Medel, and Aaron S Dumont. 2014. 'Vascular smooth muscle cells in cerebral aneurysm pathogenesis', *Translational stroke research*, 5: 338-46.
- Tal, Ofir, and Shye Shapira. 2019. "Early Diagnosis of Stroke and Internal Hemorrhage via Deep Neural Network Inference of Microwave Signals." In *2019 IEEE International Conference on Microwaves, Antennas, Communications and Electronic Systems (COMCAS)*, 1-4. IEEE.
- Tatu, Laurent, Thierry Moulin, and Guy Monnier. 2005. 'The Discovery of Encephalic Arteries From Johann Jacob Wepfer to Charles Foix', *Cerebrovascular diseases*, 20: 427-32.
- Tiwari, Varun Kumar, Mahmoud Meribout, Khalid Alhammadi, Naji Al Sayari, and Lyes Khezzar. 2023. 'A novel neural network-based data acquisition system targeting high-speed electrical impedance tomography systems', *Authorea Preprints*.
- Vesalius, Andreas. 1543. 'De humani corporis', *Basel: Fabrica*, 1547: 1543.
- Vonk-Noordegraaf, Anton, André Janse, Johan T Marcus, Jean GF Bronzwaer, Pieter E Postmus, Theo JC Faes, and Peter MJM De Vries. 2000. 'Determination of stroke volume by means of electrical impedance tomography', *Physiological measurement*, 21: 285.
- Wang, Feng, Haisheng Zhang, Junlin Bao, Huaiqiang Li, Weihao Peng, Jia Xu, Jun Yang, Wei Zhuang, Xu Ning, and Lin Xu. 2020. 'Experimental study on differential diagnosis of

- cerebral hemorrhagic and ischemic stroke based on microwave measurement', *Technology and Health Care*, 28: 289-301.
- Wang, Lei, Wen-Bo Liu, Xiao Yu, Can-Hua Xu, Xiu-Zhen Dong, and Feng Gao. 2016. "Image monitoring for head phantom of Intracranial Hemorrhage using electrical impedance tomography." In *2016 Progress in Electromagnetic Research Symposium (PIERS)*, 1408-11. IEEE.
- Woo, Daniel, Mary E Comeau, Simone Uniken Venema, Christopher D Anderson, Matthew Flaherty, Fernando Testai, Steven Kittner, Michael Frankel, Michael L James, and Gene Sung. 2022. 'Risk factors associated with mortality and neurologic disability after intracerebral hemorrhage in a racially and ethnically diverse cohort', *JAMA network open*, 5: e221103-e03.
- Woo, Daniel, Mary Haverbusch, Padmini Sekar, Brett Kissela, Jane Khoury, Alexander Schneider, Dawn Kleindorfer, Jerzy Szaflarski, Arthur Pancioli, and Edward Jauch. 2004. 'Effect of untreated hypertension on hemorrhagic stroke', *Stroke*, 35: 1703-08.
- Xu, Rui, Wei Zhuang, Zelin Bai, Feng Wang, Mingsheng Chen, Nan Liu, and Gui Jin. 2023. 'A pilot study on intracerebral hemorrhage imaging based on electrical capacitance tomography', *Frontiers in Physics*, 11: 1165727.
- Zhang, Haisheng, Mingsheng Chen, Gui Jin, Jia Xu, and Mingxin Qin. 2019. 'Experimental study on the detection of cerebral hemorrhage in rabbits based on broadband antenna technology', *Computer Assisted Surgery*, 24: 96-104.

Table 1

Table of referenced Studies

TABLE 1

Table of reference for all studies referred to in the literature review.

Reference	Title	Operating Principle	Study Type	Methods and Sample	Results and Conclusion	Strengths	Limitations
(Shi, Tian, and Wang 2021)	Simultaneous Imaging of Intracerebral Hemorrhage and Secondary Ischemia with Electrical Impedance Tomography	Impedance-based	Numerical	A numerical study investigating the use of EIT for simultaneous reconstruction of hemorrhage and ischemia.	Proposed a novel superimposed imaging method, showing improved image quality for simultaneous hemorrhage and ischemia.	Improved image quality for simultaneous hemorrhage and ischemia reconstruction using a novel superimposed imaging method.	Numerical-only study without experimental validation; effectiveness declines with reduced lesion spacing.
(Wang et al. 2016)	Image Monitoring for Head Phantom of Intracranial Hemorrhage Using Electrical Impedance Tomography	Impedance-based	Benchtop	EIT was used to detect impedance changes in head phantoms of ICH, simulating the process by injecting animal blood to monitor impedance changes in real time.	The study found that impedance changes were sensitive to the injected blood, showing different trends depending on the presence of a craniotomy, suggesting potential applications for	Demonstrated the sensitivity of EIT to real-time impedance changes using a realistic head phantom model for ICH, showing different trends depending on	The study was conducted on phantoms only, which lack the complexity of in vivo conditions; opposite trends due to craniotomy make it challenging to generalize to

Table 1

Reference	Title	Operating Principle	Study Type	Methods and Sample	Results and Conclusion	Strengths	Limitations
					early ICH diagnosis.	craniotomy presence.	clinical scenarios.
<b>(Dowrick, Blochet, and Holder 2015)</b>	In Vivo Bioimpedance Changes During Stroke and Epilepsy in the Rat Brain	Impedance-based	Animal	Bioimpedance measurements were taken in rat models during stroke and epilepsy events.	Conductivity changes correlated with stroke and seizure activities, suggesting EIT as a useful monitoring tool.	First in vivo study to differentiate bioimpedance changes between stroke and epilepsy using a rat model, showing the potential of EIT for real-time monitoring.	Limited to small animal models, which may not fully capture the complexity of human cerebral physiology; results need further validation in larger animals or clinical settings.
<b>(Murphy et al. 2022)</b>	Detection of Subclinical Hemorrhage Using Electrical Impedance: A Porcine Study	Impedance-based	Animal	Electrical impedance measurements were used to detect subclinical hemorrhage in a porcine model by creating an extended period of hemorrhage without	Demonstrated superior early detection of hemorrhage compared to standard clinical metrics, achieving an AUC of 0.96 at 80 ml bleed without requiring image	Achieved high AUC (0.96) for early hemorrhage detection, outperforming standard clinical metrics without image reconstruction .	Conducted on a porcine model; generalizability to humans is uncertain, especially for severe hemorrhage cases.

Table 1

Reference	Title	Operating Principle	Study Type	Methods and Sample	Results and Conclusion	Strengths	Limitations
				significant changes in heart rate and blood pressure.	reconstructions .		
<b>(Park et al. 2024)</b>	Analysis of Hemodynamics and Impedance Using Bioelectrical Impedance Analysis in Hypovolemic Shock-Induced Swine Model	Impedance-based	Animal	Conducted bioelectrical impedance analysis to evaluate changes in impedance in a hypovolemic shock-induced swine model; different fluid resuscitation protocols were tested.	Balanced crystalloid + 20% albumin was most effective in restoring hemodynamic parameters; impedance analysis correlated with changes in SV and MAP.	Effective non-invasive impedance monitoring correlated with hemodynamic changes in swine during hypovolemic shock.	Small sample size and controlled conditions limit generalizability to real-world clinical settings.
<b>(Chen, Tan, and Dong 2020)</b>	Excitation Strategy Analysis of Magnetic Induction Tomography for Intracranial Hemorrhage Detection	Inductance-based	Numerical	Analyzed various excitation strategies for improving the accuracy of Magnetic Induction Tomography (MIT) for detecting intracranial hemorrhage.	Identified optimal excitation configurations for improving image sensitivity and accuracy in MIT; demonstrated through numerical simulations.	Identified optimal excitation strategies for MIT, improving image sensitivity and accuracy for intracranial hemorrhage detection through a	The study is purely numerical, lacking validation with physical experiments or clinical data, which limits real-world applicability.

Table 1

Reference	Title	Operating Principle	Study Type	Methods and Sample	Results and Conclusion	Strengths	Limitations
						numerical approach.	
<b>(Oziel, Korenstein, and Rubinsky 2018)</b>	Non-Contact Monitoring of Temporal Volume Changes of a Hematoma in the Head by a Single Inductive Coil	Inductance-based	Numerical	A numerical study using an inductive coil to monitor changes in hematoma volume in a human head model.	The inductive coil showed sensitivity to volume changes but required multi-frequency measurements for accuracy.	The inductive coil provides non-contact monitoring, is cost-effective, and has better resolution in various scenarios compared to other methods when hematoma location is not precisely known.	Highly sensitive to rotation artifacts, and requires multifrequency measurements to yield reliable diagnostic information.
<b>(Oziel, Rubinsky, and Korenstein 2020)</b>	Detection and Estimation of Blood Accumulation Volume in Brain Hemorrhage	Inductance-based	Benchtop	Changes in the scattering parameters (S21) of an inductive coil were measured in a human anatomical skull.	Found that the inductive coil could detect changes in the tissue/fluid ratio with a high level of accuracy.	Demonstrated a simple, inexpensive approach with an inductive coil that effectively detects changes in the tissue/fluid ratio in a realistic head model,	The method requires further development to address motion artifacts, lacks clinical validation, and experiments were limited to static laboratory conditions without

Table 1

Reference	Title	Operating Principle	Study Type	Methods and Sample	Results and Conclusion	Strengths	Limitations
						achieving 90% accuracy.	accounting for real-life variability.
(Bai et al. 2019)	Detection of Rabbit Intracranial Hemorrhage Based on Permittivity	Inductance-based	Animal	A single excitation coil and receiving coil were used to measure the real part of $\Delta B/B$ to evaluate the amount of bleeding in rabbit heads.	The real part data showed a significant decline during blood injection, indicating feasibility for detecting intracerebral hemorrhage.	Introduced a more sensitive permittivity-based approach for ICH detection, successfully distinguishing blood from other solutions and demonstrating feasibility in animal models.	Limited to animal testing; calibration challenges and individual physiological variations may affect human applicability.
(Li et al. 2022)	Early Assessment of Acute Ischemic Stroke in Rabbits Based on Multi-Parameter Near-Field Coupling Sensing	Inductance-based	Animal	A multi-parameter NFC sensing system was used for early assessment of AIS in rabbits by measuring phase and amplitude changes.	Demonstrated the feasibility of using NFC for dynamic AIS monitoring; achieved 100% classification accuracy using BP network.	Achieved 100% classification accuracy using multi-parameter NFC sensing for non-invasive, real-time monitoring of ischemic events.	Requires precise frequency selection, and results may be sensitive to physiological differences not captured in controlled animal models, limiting generalizability

Table 1

Reference	Title	Operating Principle	Study Type	Methods and Sample	Results and Conclusion	Strengths	Limitations
							to diverse human conditions.
(Bai et al. 2021)	Research on the Measurement of Intracranial Hemorrhage in Rabbits by a Parallel-Plate Capacitor	Capacitance-based	Animal	A self-made parallel plate capacitor was used to detect changes in the blood/tissue volume ratio in rabbits.	Capacitance increased with the volume of blood injected, demonstrating feasibility for non-invasive detection of hemorrhage.	Demonstrated effectiveness of a parallel-plate capacitor in distinguishing liquids by permittivity, supporting non-invasive hemorrhage detection.	Significant variability among animals and use of heparin-treated blood may affect generalizability to natural hemorrhage conditions
(Xu et al. 2023)	A Pilot Study on Intracerebral Hemorrhage Imaging Based on Electrical Capacitance Tomography	Capacitance-based	Numerical , Ex Vivo	A 16-electrode ECT system was used for two-dimensional imaging of ICH; conducted on a 5-layer spherical numerical model and an ex vivo porcine brain model.	Successfully demonstrated imaging of bleeding in numerical and ex vivo models, though positional accuracy was off by 3 mm in ex vivo experiments.	Demonstrated effective bleeding detection with improved spatial resolution using a 16-electrode ECT system in both simulations and ex vivo pig brain models.	Positional inaccuracy of 3 mm and insufficient imaging resolution limit clinical applicability.
(Huang et al. 2024)	Research on Electrical	Capacitance-based	Numerical ,	A study investigating	Demonstrated absolute	Effective symmetrical	Imaging quality highly

Table 1

Reference	Title	Operating Principle	Study Type	Methods and Sample	Results and Conclusion	Strengths	Limitations
	Capacitance Tomography (ECT) Detection of Cerebral Hemorrhage Based on Symmetrical Cancellation Method		Benchtop, Animal	the use of a symmetrical cancellation method in ECT for detecting ICH; included numerical simulation, benchtop models, and animal experiments.	imaging of ICH with symmetrical cancellation, though a mirrored artifact was observed; results indicate potential for prehospital emergency applications.	cancellation imaging allows for absolute imaging of ICH without pre-hemorrhage data, improving practical applicability for prehospital and emergency scenarios.	depends on precise electrode alignment, and mirrored artifacts appear, which complicates interpretation.
<b>(Peng et al. 2023)</b>	Study on Detection of Intracerebral Hemorrhage Based on Frequency Difference of Permittivity	Capacitance -based	Numerical , Benchtop, Animal	Introduced a novel approach using the frequency-dependent variations in permittivity to detect ICH; tested on single-component substances (distilled water, sheep blood, pig fat, pig	Identified optimal frequency bands for detecting blood in different tissues. Demonstrated that absolute ICH detection is feasible through permittivity differences.	Novel frequency-dependent permittivity method effectively differentiated hemorrhage without needing baseline data.	Used treated and frozen samples, which may not fully represent in vivo conditions.

Table 1

Reference	Title	Operating Principle	Study Type	Methods and Sample	Results and Conclusion	Strengths	Limitations
				brain) and mixtures involving blood.			
<b>(Che et al. 2023)</b>	Noninvasive Image Reconstruction of Flowing Thrombus With Electrical Capacitance Tomography	Capacitance-based	Numerical , Benchtop, Animal	Developed an eight-electrode ECT system for noninvasive, real-time detection of flowing thrombus; conducted dynamic experiments using fresh porcine blood clots.	Demonstrated the feasibility of using ECT for in vitro thrombus detection, with effective target identification through sum of voltage curves and real-time imaging.	Effective real-time thrombus detection with an eight-electrode ECT system, achieving dynamic imaging with a speed of 40 frames per second.	Sensor design requires optimization for better anti-interference capabilities, and multitarget detection needs further research.
<b>(Alon and Dehkharghani 2021)</b>	A Stroke Detection and Discrimination Framework Using Broadband Microwave Scattering on Stochastic Models with Deep Learning	Radio Frequency Based	Numerical	Investigated microwave scattering perturbations using ultra wide-band antenna arrays to learn dielectric signatures of hemorrhagic strokes; used	Achieved >94% accuracy in stroke detection using DNNs trained on microwave scattering data; showed potential for intelligent diagnostics without conventional	Achieved high classification accuracy (94.6%) and precise localization of hemorrhagic stroke using microwave scattering data, demonstrating the feasibility	Relied on 2D simulations instead of 3D, which limits the physiological realism; the study's findings need to be validated through experimental

Table 1

Reference	Title	Operating Principle	Study Type	Methods and Sample	Results and Conclusion	Strengths	Limitations
				2D stochastic head models.	image formation.	of a novel, non-invasive diagnostic approach for stroke detection.	and in vivo human trials.
<b>(Rodriguez-Duarte et al. 2021)</b>	Experimental Validation of a Microwave System for Brain Stroke 3-D Imaging	Radio Frequency Based	Benchtop	Experimental validation of a microwave imaging system for 3-D imaging of brain stroke using a head phantom and ex vivo calf brains to mimic hemorrhagic and ischemic conditions.	Demonstrated successful localization of hemorrhagic and ischemic strokes using microwave imaging with a differential approach, though resolution remained lower compared to conventional imaging techniques.	The microwave imaging system effectively localizes hemorrhagic and ischemic strokes with a low-complexity design, making it suitable for continuous bedside monitoring.	Limited resolution compared to established imaging methods like MRI, and variability in antenna placement may impact the accuracy of measurements.
<b>(Wang et al. 2020)</b>	Experimental Study on Differential Diagnosis of Cerebral Hemorrhagic and Ischemic Stroke Based	Radio Frequency Based	Animal	Investigated early, noncontact identification of hemorrhagic vs. ischemic stroke using microwave	Achieved 93.75% accuracy in identifying hemorrhagic stroke with 2 ml blood loss and 91.7%	High accuracy for differentiating hemorrhagic and ischemic strokes using a portable, non-invasive	The small sample size (14 rabbits) limits generalizability, and electromagnetic interference in the

Table 1

Reference	Title	Operating Principle	Study Type	Methods and Sample	Results and Conclusion	Strengths	Limitations
	on Microwave Measurement			scattering parameters measured in rabbit models.	accuracy in identifying ischemic stroke with an ischemic interval of 42 minutes; demonstrated the potential for a portable, noninvasive prehospital diagnostic system.	microwave system.	experimental setup affected measurement stability.
(Zhang et al. 2019)	Experimental Study on the Detection of Cerebral Hemorrhage in Rabbits Using Broadband Antenna	Radio Frequency Based	Animal	A microstrip antenna was used to monitor changes in the electromagnetic properties in a rabbit model.	Detected phase difference changes with increased bleeding volume, showing promise for non-contact monitoring.	Demonstrated feasibility of microwave-based hemorrhage detection with 77% accuracy in rabbits.	Moderate accuracy and lack of consistency limit clinical applicability.
(Tal and Shapira 2019)	Early Diagnosis of Stroke and Internal Hemorrhage via Deep Neural	Radio Frequency Based	Numerical , Benchtop	Investigated microwave sensing combined with deep neural network inference for	Achieved 90% sensitivity for hemorrhage larger than 0.5 ml and demonstrated the feasibility	Acceptable sensitivity for hemorrhagic stroke detection using a compact,	Limited to simulations and phantoms, restricting real-world applicability.

Table 1

Reference	Title	Operating Principle	Study Type	Methods and Sample	Results and Conclusion	Strengths	Limitations
	Network Inference of Microwave Signals			detecting brain stroke and internal abdominal hemorrhage; tested on electromagnetic simulations and physical phantoms.	of a compact, autonomous system suitable for out-of-hospital environments.	autonomous microwave system.	

## Table 1

### References

- Alon, Leeor, and Seena Dehkharghani. 2021. 'A stroke detection and discrimination framework using broadband microwave scattering on stochastic models with deep learning', *Scientific reports*, 11: 24222.
- Bai, Zelin, Haocheng Li, Jingbo Chen, Wei Zhuang, Gen Li, Mingsheng Chen, Jia Xu, Shuanglin Zhao, Yuening Liu, and Jian Sun. 2021. 'Research on the measurement of intracranial hemorrhage in rabbits by a parallel-plate capacitor', *PeerJ*, 9: e10583.
- Bai, Zelin, Qingguang Yan, Gen Li, Wei Zhuang, Jingbo Chen, Jun Yang, Jia Xu, Lin Lu, Mingsheng Chen, and Lin Xu. 2019. 'Detection of rabbit intracranial hemorrhage based on permittivity', *Measurement Science and Technology*, 30: 115701.
- Che, Quanqi, Hao Wang, Zhiwei Li, Hongtao Wu, Bai Chen, Kai Liu, and Jiafeng Yao. 2023. 'Noninvasive Image Reconstruction of Flowing Thrombus With Electrical Capacitance Tomography', *IEEE Sensors Journal*, 23: 5949-55.
- Chen, Yixuan, Chao Tan, and Feng Dong. 2020. "Excitation Strategy Analysis of Magnetic Induction Tomography for Intracranial Hemorrhage Detection." In *2020 39th Chinese Control Conference (CCC)*, 2780-85. IEEE.
- Dowrick, T, C Blochet, and D Holder. 2015. 'In vivo bioimpedance measurement of healthy and ischaemic rat brain: implications for stroke imaging using electrical impedance tomography', *Physiological measurement*, 36: 1273-82.
- Huang, Jing, Feng Chen, Ke Wang, and Sheng Chen. 2024. 'Research on electrical capacitance tomography (ECT) detection of cerebral hemorrhage based on symmetrical cancellation method', *Frontiers in Physics*, 12: 1392767.

Table 1

- Li, Gen, Shengtong Yin, Man Jian, Jingbo Chen, Lingxi Zeng, Zelin Bai, Wei Zhuang, Bingxin Xu, Shengjie He, and Jian Sun. 2022. 'Early assessment of acute ischemic stroke in rabbits based on multi-parameter near-field coupling sensing', *BioMedical Engineering OnLine*, 21: 1-19.
- Murphy, Ethan K, Samuel B Klein, Alexandra Hamlin, Justin E Anderson, Joseph M Minichiello, Alexander L Lindqwister, Karen L Moodie, Zachary J Wanken, Jackson T Read, and Victor A Borza. 2022. 'Detection of subclinical hemorrhage using electrical impedance: a porcine study', *Physiological measurement*, 43: 055001.
- Oziel, Moshe, Rafi Korenstein, and Boris Rubinsky. 2018. 'Non-contact monitoring of temporal volume changes of a hematoma in the head by a single inductive coil: a numerical study', *IEEE Transactions on Biomedical Engineering*, 66: 1328-36.
- Oziel, Moshe, Boris Rubinsky, and Rafi Korenstein. 2020. 'Detection and estimating the blood accumulation volume of brain hemorrhage in a human anatomical skull using a RF single coil', *PeerJ*, 8: e10416.
- Park, Hoonsung, Hanyoung Lee, Seungmin Baik, and Jae-Myeong Lee. 2024. 'Analysis of hemodynamics and impedance using bioelectrical impedance analysis in hypovolemic shock-induced swine model', *Scientific reports*, 14: 15077.
- Peng, Shixin, Xiaoshu Wang, Gui Jin, Feng Wang, Ji Zhu, Xiaodong Zhang, Nan Liu, and Rui Xu. 2023. 'Study on detection of intracerebral hemorrhage based on frequency difference of permittivity', *Frontiers in Physics*, 11: 1333185.
- Rodriguez-Duarte, David O, Jorge A Tobon Vasquez, Rosa Scapaticci, Giovanna Turvani, Marta Cavagnaro, Mario R Casu, Lorenzo Crocco, and Francesca Vipiana. 2021. 'Experimental validation of a microwave system for brain stroke 3-d imaging', *Diagnostics*, 11: 1232.
- Shi, Yanyan, Zhiwei Tian, and Meng Wang. 2021. "Simultaneous Imaging of Intracerebral Hemorrhage and Secondary Ischemia with Electrical Impedance Tomography." In *2021 IEEE International Conference on Consumer Electronics and Computer Engineering (ICCECE)*, 723-26. IEEE.

Table 1

- Tal, Ofir, and Shye Shapira. 2019. "Early Diagnosis of Stroke and Internal Hemorrhage via Deep Neural Network Inference of Microwave Signals." In *2019 IEEE International Conference on Microwaves, Antennas, Communications and Electronic Systems (COMCAS)*, 1-4. IEEE.
- Wang, Feng, Haisheng Zhang, Junlin Bao, Huaiqiang Li, Weihao Peng, Jia Xu, Jun Yang, Wei Zhuang, Xu Ning, and Lin Xu. 2020. 'Experimental study on differential diagnosis of cerebral hemorrhagic and ischemic stroke based on microwave measurement', *Technology and Health Care*, 28: 289-301.
- Wang, Lei, Wen-Bo Liu, Xiao Yu, Can-Hua Xu, Xiu-Zhen Dong, and Feng Gao. 2016. "Image monitoring for head phantom of Intracranial Hemorrhage using electrical impedance tomography." In *2016 Progress in Electromagnetic Research Symposium (PIERS)*, 1408-11. IEEE.
- Xu, Rui, Wei Zhuang, Zelin Bai, Feng Wang, Mingsheng Chen, Nan Liu, and Gui Jin. 2023. 'A pilot study on intracerebral hemorrhage imaging based on electrical capacitance tomography', *Frontiers in Physics*, 11: 1165727.
- Zhang, Haisheng, Mingsheng Chen, Gui Jin, Jia Xu, and Mingxin Qin. 2019. 'Experimental study on the detection of cerebral hemorrhage in rabbits based on broadband antenna technology', *Computer Assisted Surgery*, 24: 96-104.

## CHAPTER III

### Classification of the Rate of Growth of a Phantom Cerebral Hemorrhage in an Ex Vivo Porcine Model via a Radio Frequency Resonator

#### Abstract

Secondary hematoma expansion following the initial bleeding event significantly increases the risk of death and disability. This study focuses on developing a method for continuous, non-invasive monitoring of hematoma expansion using a radio frequency (RF) resonator. Flow rates of saline, ranging from 0 to 20 mL, were detected using an intact porcine head model to simulate the effects of hematoma expansion. The sensor was positioned along the mid-sagittal plane, with placement optimized based on resonant frequency shifts correlated to changes in volume.

RF sweeps were performed, and the complex S11 scattering parameter was collected. The magnitude, phase and imaginary component were extracted from the sweeps. These data were then used to create images representing time, frequency, and response characteristics, forming the input for a convolutional neural network (CNN). The CNN was trained to classify flow rates with accuracies as high as 96.7%, demonstrating the feasibility of this RF-based approach for early detection and monitoring of hematoma growth.

#### Introduction

The initial stage of hematoma formation displays a growth period to a baseline volume within the first few hours after onset. After the initial growth period, a secondary growth phase may follow. Initial hematoma volume and rate of growth both correlate positively with secondary

hematoma expansion (Brouwers and Greenberg 2013). Secondary hematoma expansion is associated with poor health outcomes, as a 10% increase in mortality is associated with every 5% increase in hematoma volume. Additionally, every milliliter increase in volume increases the chance of severe disability as a health outcome by 7% (LoPresti et al. 2014).

Current imaging methods are limited by safety concerns or impracticality for continuous, non-invasive monitoring of hematoma progression, particularly during the critical early hours after onset when patients are in transit or in regions with low-resource availability. CT and MRI are insufficient for continuous monitoring due to factors such as cost, limited availability, radiation exposure, and the need for highly trained personnel to operate the equipment (Mohammadshahi et al. 2019; Nowinski 2024). Positron emission tomography (PET), though preferred for detecting changes in metabolism due to ischemia, has no place in the emergency setting and requires exposure to radiation (Chalet et al. 2022). Additionally, current imaging modalities such as Transcranial Doppler (TCD), Digital Subtraction Angiography (DSA), and Single-Photon Emission Computed Tomography (SPECT) are limited by issues such as operator dependence, invasiveness, and poor spatial resolution (Nowinski 2024). This disparity in access to adequate imaging and monitoring is especially pronounced in low-resource settings, where patients often face significant challenges in receiving timely and effective care during transport and upon reaching medical facilities (Ikeme et al. 2022).

In this chapter, the feasibility of a method for continuously monitoring changes in hematoma growth rate using a monostatic radio frequency resonator is investigated. Radio frequency sweeps are impinged upon the resonator and the complex  $S_{11}$  scattering parameters are recorded. Previous work in our lab has used this methodology, demonstrating its promise in non-invasive monitoring of internal physiological parameters. Applications have included measuring

stroke volume, hemodynamics and intracranial fluid shifts(Alruwaili et al. 2018; Becker 2019; Cluff et al. 2017; Griffith et al. 2018; Griffith et al. 2023; Loflin et al. 2020; Mohammed et al. 2019; Mohammed et al. 2022; Schmidt et al. 2022). The magnitude, phase, and imaginary component are extracted from these sweeps. These data are then used to create images where time is represented by the height, frequency represents the width. The magnitude, phase, and imaginary component comprise the three channels of the images. Finally, a CNN is trained to classify these images by their flow rate.

## Methods

### *Resonating Sensor and Experimental Design*

The resonating sensor is composed of a spiral planar copper trace, surrounded by a simple loop antenna. The loop trace is 2 mm wide. The spiral trace is 1.5 mm wide, with a 0.5 mm gap between adjacent traces. There are 9 spiral traces in total. The gap between the outer edge of the spiral and the loop antenna is 1 mm (Figure 11).

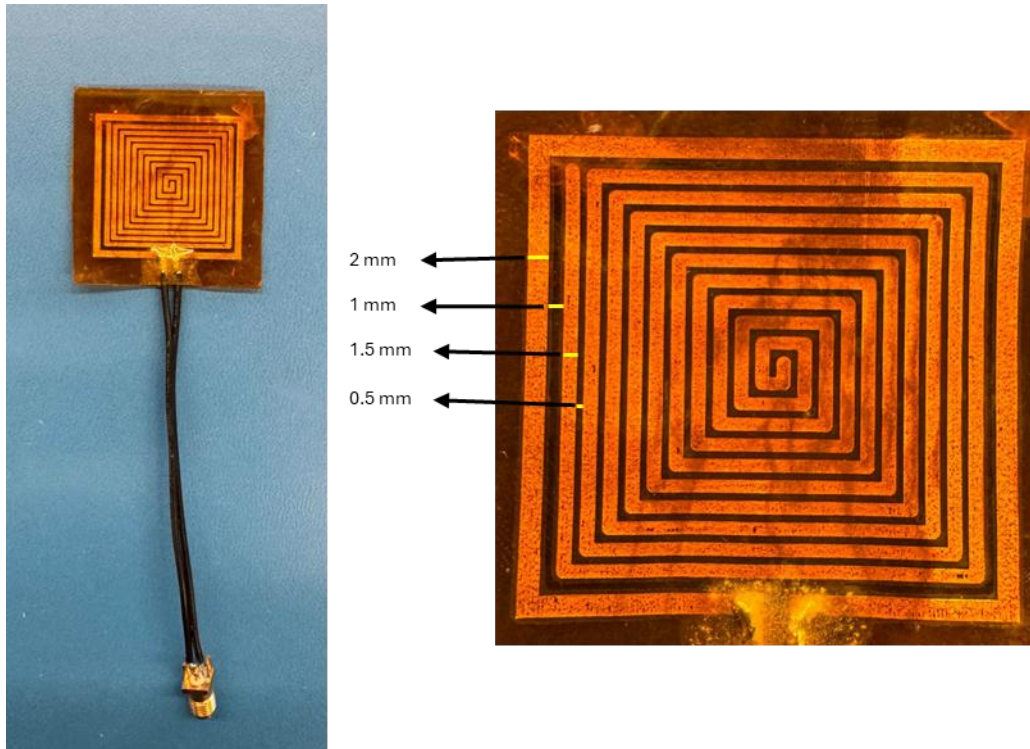


Figure 11: The loop trace, spiral trace, trace gas, and the gap between the gap along the spiral measure 2 mm, 1.5 mm, 0.5 mm, and 1 mm respectively. There are nine turns within the spiral pattern.

Using a vector network analyzer (VNA) (LibreVNA), sweeps with the following parameters were conducted throughout the experiment: range from 200 MHz - 2GHz, with an intermediate frequency bandwidth (IFBW) of 50 kHz, and 4001 data points. The IFBW is suggested to be ~10% of the frequency span between data points in order to optimize the signal to noise ration. Since the span between data points is ~450,000 Hz, an IFBW of 50 kHz was chosen. Prior to every experiment, the VNA was calibrated using the short, open, load (50 Ohm) single port calibration standards included with the LibraVNA kit. The collected parameters are as follows:  $S_{11}$  complex scattering parameter, per sweeps time stamps, and frequency.

## *Theoretical Background*

RF resonators operate based on the principle of electromagnetic resonance, where an RF signal induces an oscillating electromagnetic field within the resonator structure. The frequency at which resonance occurs is influenced by both the geometry of the resonator and the dielectric properties of the surrounding environment. These resonators generate an electromagnetic field that interacts with biological tissues, and their resonant properties are sensitive to the effective permittivity of the material being probed.

The resonant frequency is determined by the inductive and capacitive components of the resonator. When a biological material, such as tissue or fluid, comes into contact with the resonator's field, the dielectric properties of that material influence the capacitance, thereby shifting the resonant frequency. This sensitivity to permittivity makes RF resonators particularly useful in detecting changes in fluid content, such as intracranial hemorrhages, where blood volume changes significantly alter the local dielectric properties. The equations for the inductance (L), capacitance (C<sub>-1</sub>), and the resonant frequency (f) are shown below:

$$L = \frac{\mu_0}{4\pi I^2} \iiint \frac{[J(r_i) \cdot \mu_i][J(r_j) \cdot \mu_j]}{|r_i - r_j|} d^3r_i d^3r_j$$

Equation 5

$$C_{-1} = \frac{1}{4\epsilon_0 Q^2} \iiint \frac{\rho(r_i) \cdot \rho(r_j) \cdot k_{ij}}{|r_i - r_j|} d^3r_i d^3r_j$$

Equation 6

$$f = \frac{1}{2\pi\sqrt{LC}}$$

Equation 7

In these equations, L represents the total inductance of the resonator, which depends on the spatial current density,  $J(r)$ , and the permeability,  $\mu$ , of the medium. The term  $\mu_0$  is the magnetic permeability of free space, I is the total current in the circuit, and  $r_i, r_j$  represent spatial coordinates. The reciprocal capacitance,  $C_{-1}$ , involves  $\rho(r_i)$ , the spatial charge density, and  $\epsilon_0$ , the electrical permittivity of free space. The factor  $k_{ij}$  represents the geometric configuration of the resonator elements, while Q is the quality factor of the resonator. Finally, the resonant frequency f is determined by the interplay between inductance and capacitance (Szatkowski et al. 2014) (Woodard 2011, 2010) .

### *Porcine Model*

The hemorrhagic stroke was simulated using pig head donated by a local butcher (Stroots; Mulvane, Ks). IACUC approval of our tissue protocol was obtained prior to conducting the study. The experiment consisted of 8 replicants. The distance from the apex of the head to the end of the snout, and the distance from the outside corner of each eye is measure per replicate. 20 ml of 1% saline solution was injected at continuous rate into a small latex blood which as placed into the mid brain via the foramen magnum (Figure 12).

TABLE 2

Anatomical metrics of each replicant

Replicate #	Apex - snout	Eye - eye
1	28.75 cm*	16.6 cm*
2	27 cm	17cm
3	28.5 cm	16.5 cm
4	28.8 cm*	16.6 cm*
5	30 cm	16 cm
6	25 cm	15 cm
7	31 cm	18 cm
8	31 cm	17 cm

Missing data filled with the mean.\*

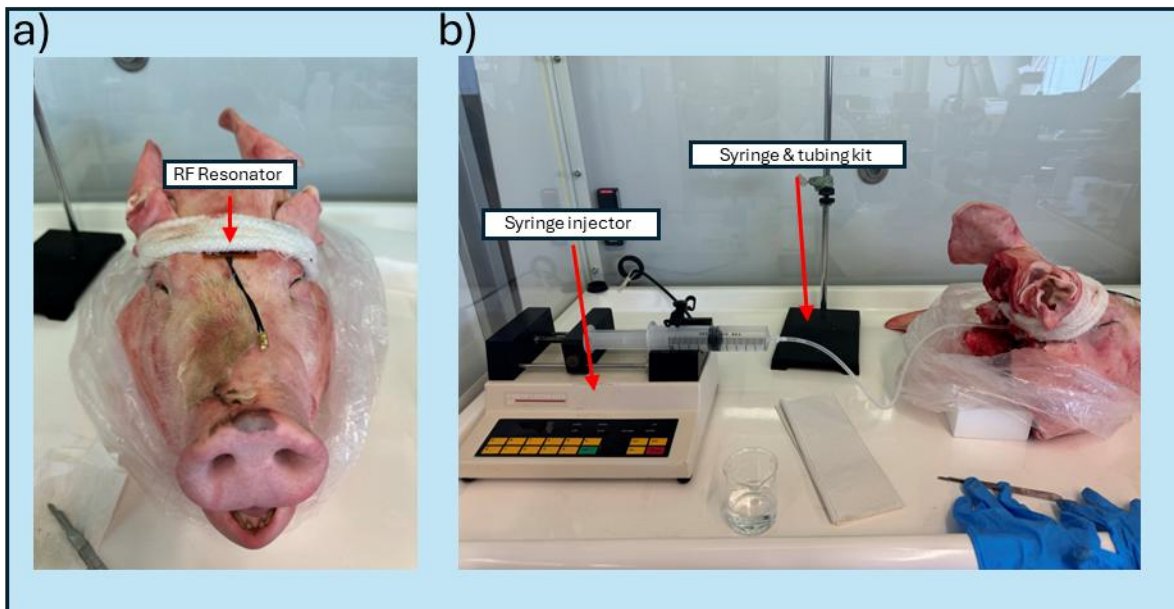


Figure 12: The sensor is held in place by a cloth band which wraps around the head (a). The experimental set up consisting of the tubing kit and syringe injector (b).

5 flow rates: 0, 1, 2, 4, 5 ml/min. These flow rates were selected so that an equal number of samples may be generated while keeping the representation of total volume the same. In other words, each flow rate divides evenly into 20 ml. A single 20-minute collection at 1 ml/min, two 10-minute collections at 2 ml/min, and so on until an equal number of samples (time) are collected for each flow rate from 0 – 20 ml.

The position of the sensor along the mid-sagittal plane of the forehead was determined experimentally for each replicate (Figure 13).



Figure 13: Starting from the apex of the head, 5 positions are marked 5 cm apart along the mid-sagittal plane.

Four minutes of data was collected at a flow rate of 5ml/min at each position. Then, a linear model was fit for each resonant frequency and volume. The position of the sensor was then decided based on the  $R^2$  values generated from these models. Each selected position had at least one resonant frequency which displayed an  $R^2$  value of 0.7 or greater (Figure 14).

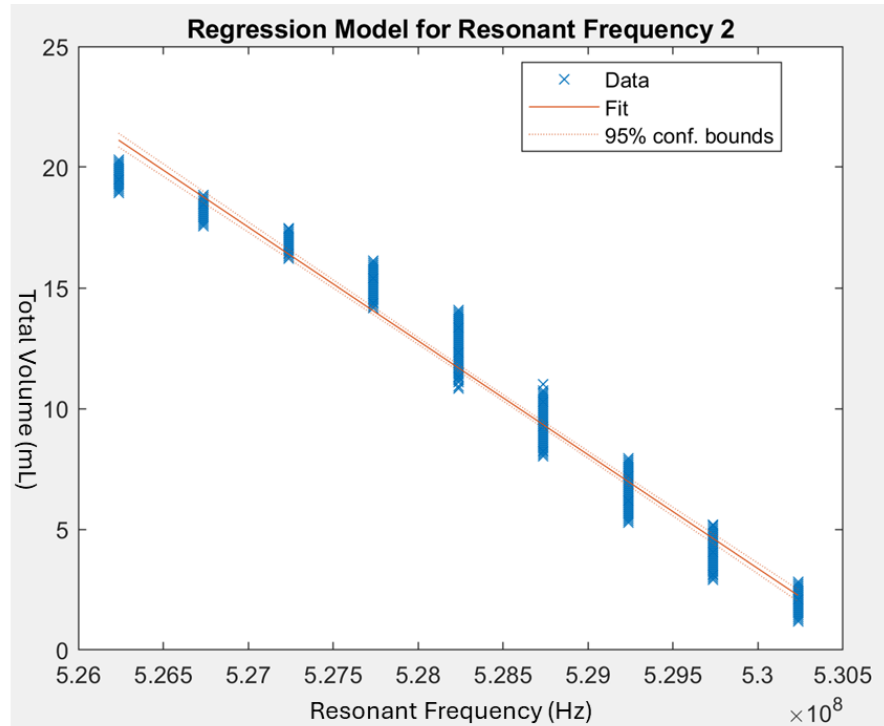


Figure 14: A linear model is fit for the second resonant frequency (x-axis) and total volume (y-axis) ( $R^2 = 0.967$ ). A leftward shift in the resonant frequency is observed as volume increases.

### *Machine Learning Models*

The resonant frequencies were identified for each frequency sweep then the shifts in these frequencies over time were calculated by taking the difference from the first sweep's resonant frequencies. Resonant frequencies were identified via the zero crossings of the imaginary component.

Across all flow rates, a minimum of 5 resonant frequencies is detected. Compared to PPG and ECG signals, few landmarks are noted in the RF sweep signal. For this reason, only the resonant frequencies are observed in this study. These data are structured into a tabular format. Linear regression models are trained using the shifts in each resonant frequency to predict volume change. All proceeding machine learning models are multivariate, incorporating the first 5 resonant

frequencies of each sweep. A multivariate linear regression model which incorporates all resonant frequencies and their shifts is trained to predict volume change.

Following the multivariate linear regression model, logistic regression, K-nearest neighbors, and random forest models are evaluated in their ability to classify flow rate. A parameter grid search was performed to determine the best hyperparameter configuration for each model. The total dataset size was 18,880 samples. Models utilized an 80:20 training-validation split. Divided evenly into 3,376 samples per class.

### *Time-Frequency Image Formation*

The raw data used in this study consisted of multiple .mat files containing sweep data. The .mat files were loaded using scipy.io to extract the sweep data and associated timestamps. The sweep data consisted of the real and imaginary component of the complex  $S_{11}$  scattering parameter and the frequency at each data point of the sweep (4001 datapoints). From this data, the magnitude and phase were calculated and selected along with the imaginary components as key features for training a deep learning model. Images were then created with the height being sweep index (time) and the width being frequency with three channels: the magnitude, phase, and imaginary component (Figure 15).

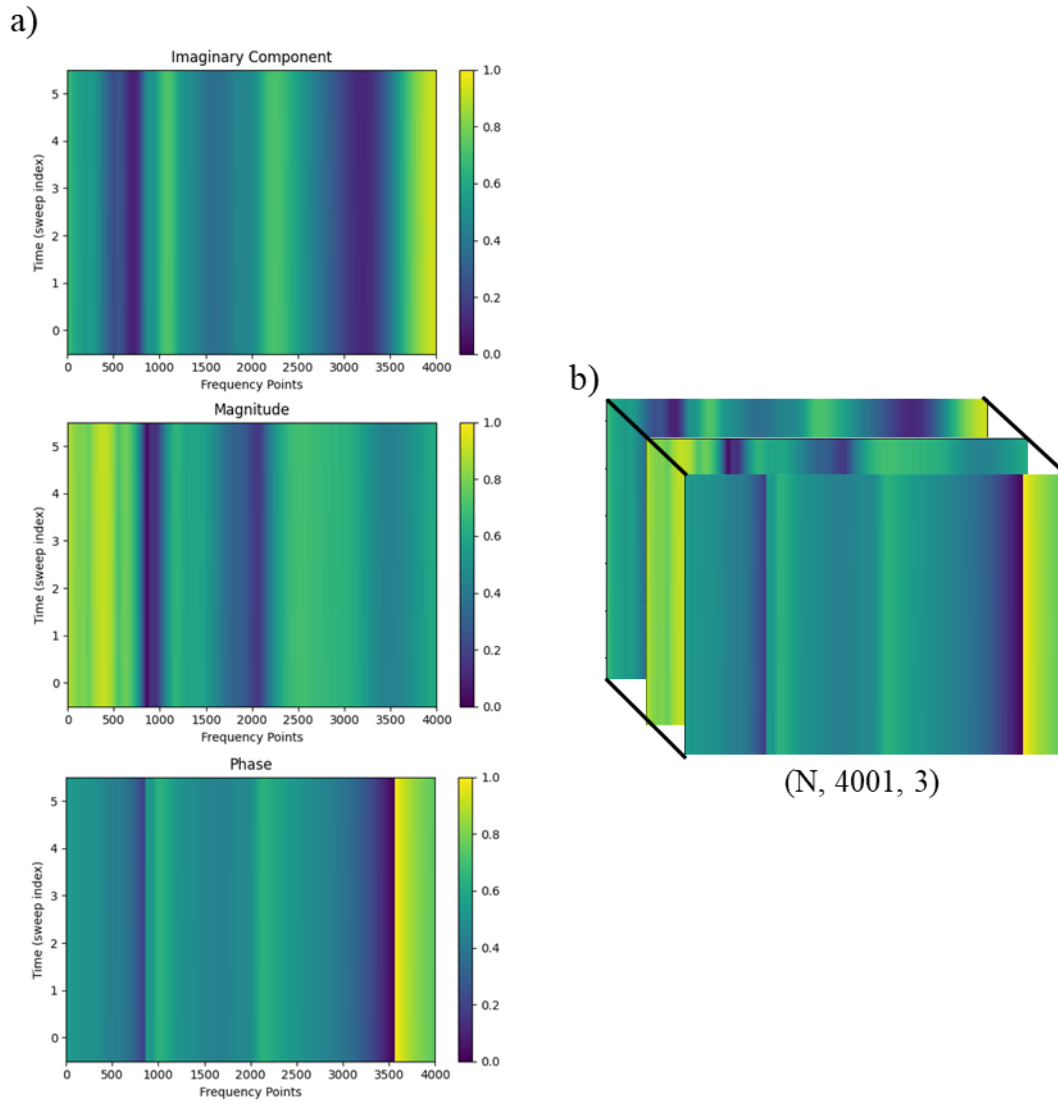


Figure 15: Time-frequency images are created of the imaginary component, magnitude, and phase (a). These features form the 3 channels of the inputted hypercubes which serve as samples for each flow rate (b).

These three features were selected for the following reasons: 1) resonant frequencies occur when the imaginary component is equal to zero, and 2) the magnitude and phase will also be altered due to the changes in the dielectric properties of the tissue. By calculating the magnitude and phase in the data processing phase, the deep learning model will not have to infer the relationship between them and the complex  $S_{11}$  scattering parameter from which they are derived. The

imaginary component is retained, as it gives the model direct access to the resonant frequency. Previous work by our lab has demonstrated that the resonant frequency shifts in response to physiological changes (Griffith et al. 2023; Griffith et al. 2016; Griffith 2019; Becker 2019; Mohammed 2019). The magnitude, phase, and imaginary component were normalized to a range of 0 – 1. Twenty minutes of data were collected for each flow rate from each replicate. For each flow rate, the data set was parsed into a matrix of dimensions:

$$N_s \text{ (samples)} \times N_t \text{ (sweep index/time)} \times 4001 \text{ (datapoints/frequency)}$$

$$\times 3 \text{ (Magnitude/Phase/Imag.)}$$

Equation 8

Where  $N_s$  is equal to the total time of flow rate data divided by the number of sweep indices used to create the image multiplied by the number of replicates.  $N_t$  is equal to the number of sweep indices used to create images. Sweep index lengths of 10 ( $N_s = 4681$ ) and 20 ( $N_s = 2313$ ) were evaluated.

### *Convolutional Neural Network Architecture*

Three CNN architectures are evaluated. These models increase in their complexity, starting with a single convolutional layer (Figure 16), then adding a second (Figure 17) and finally a third (Figure 18) convolutional layer. Each convolutional layer utilizes a ReLU activation function and is terminated by a maxpooling layer to reduce the spatial dimensions while retaining important features. The intent behind progressively increasing the number of convolutional layers was to evaluate the potential benefit of deeper architectures in extracting complex features from the generated time-frequency images.

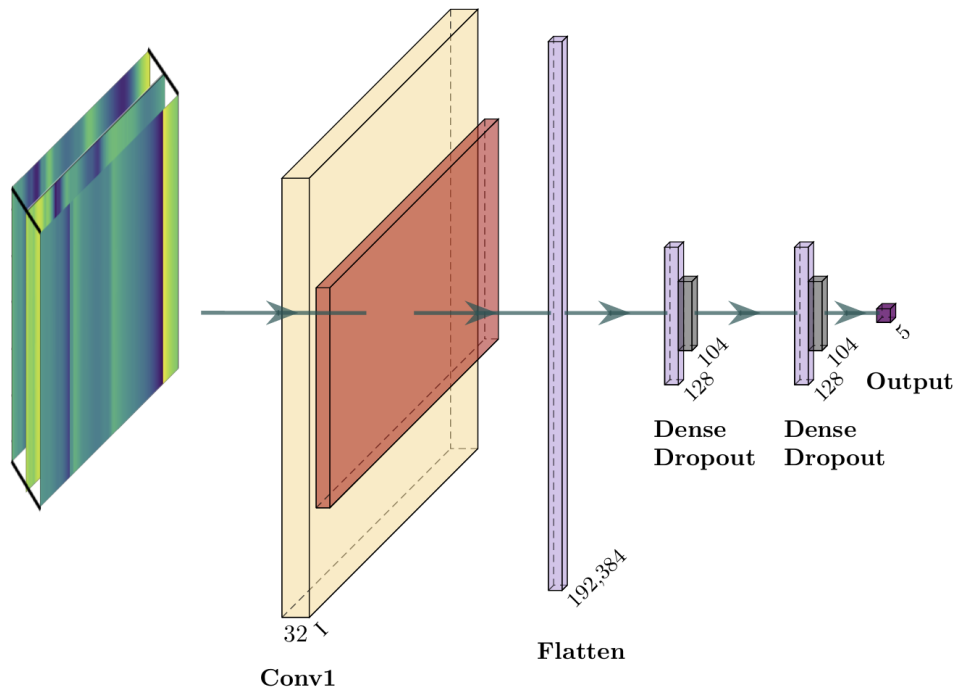


Figure 16: The architecture consists of a single convolutional layer (yellow) followed by a maxpooling layer (orange). A flattening layer (purple) and two dense-dropout (purple-black) precede the output (dark purple).

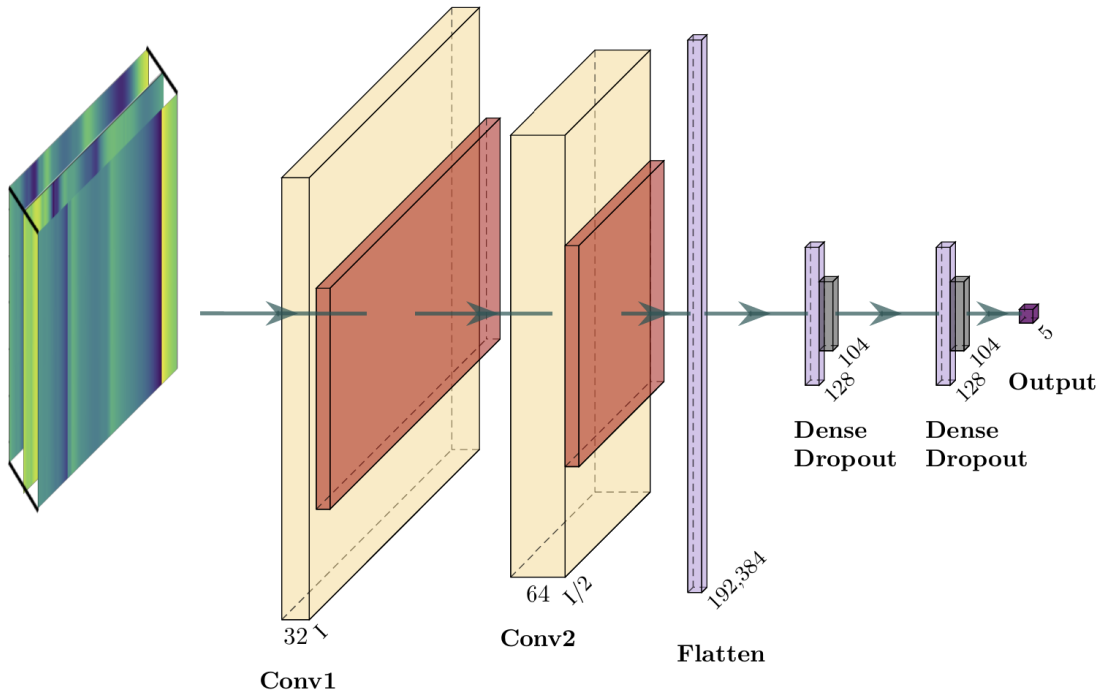


Figure 17: A second convolutional-maxpooling layer is added to the architecture.

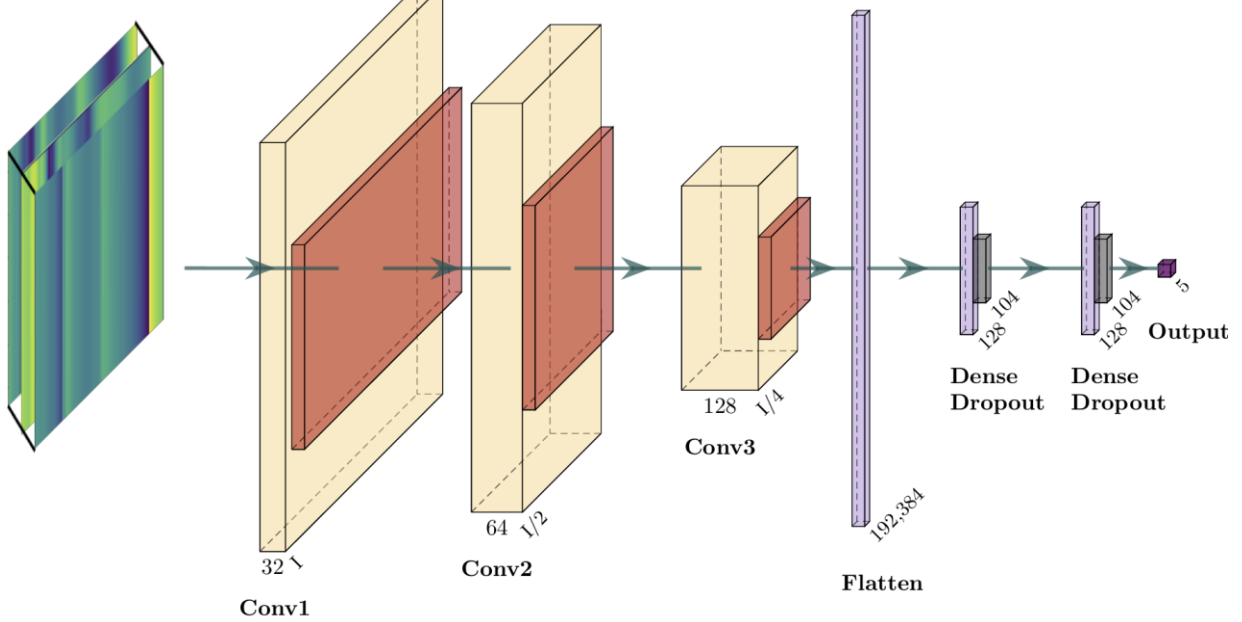


Figure 18: Finally, a third convolutional-maxpooling layer is considered.

Each convolutional layer had a kernel size of 3x3, with a stride of 1, chosen to effectively capture local spatial dependencies in the time-frequency images. Max pooling was performed with a pool size of 2x2, aiming to downsample the feature maps while reducing computation costs. The increase in the number of convolutional layers was hypothesized to improve the model's ability to extract hierarchical features from the input images, with deeper layers focusing on higher-level abstractions of the data.

After the convolutional stages, the model includes a flattening layer that reshapes the 2D feature maps into a 1D vector. This was followed by two fully connected dense layers, each with a dropout rate of 0.2 to reduce overfitting. Dropout was applied during training to randomly deactivate 20% of the neurons in the dense layers, thereby enhancing the model's generalization capabilities.

The output layer utilized a softmax activation function to produce a probability distribution for a 5-node classification (0, 1, 2, 4, and 5 ml/min). A grid search was conducted for each model to find the optimal hyperparameter configuration.

TABLE 3

Hyperparameters explored and their values.

Parameter	Values
Learning rate	[0.001, 0.01]
Dropout rate	[0.2, 0.3]
Filters	[32.0, 64.0]
Dense units	[128.0, 256.0]
Batch size	[16.0, 32.0]
Epochs	[20.0, 30.0]

Training was conducted with an 80-20 split for training and validation, respectively. The training process was monitored using categorical cross-entropy as the loss function, and accuracy was used as the primary evaluation metric. While training the model, early stopping was employed to halt training when the validation loss ceased to improve for 5 consecutive epochs, helping prevent overfitting (Figure 19 & Figure 20).

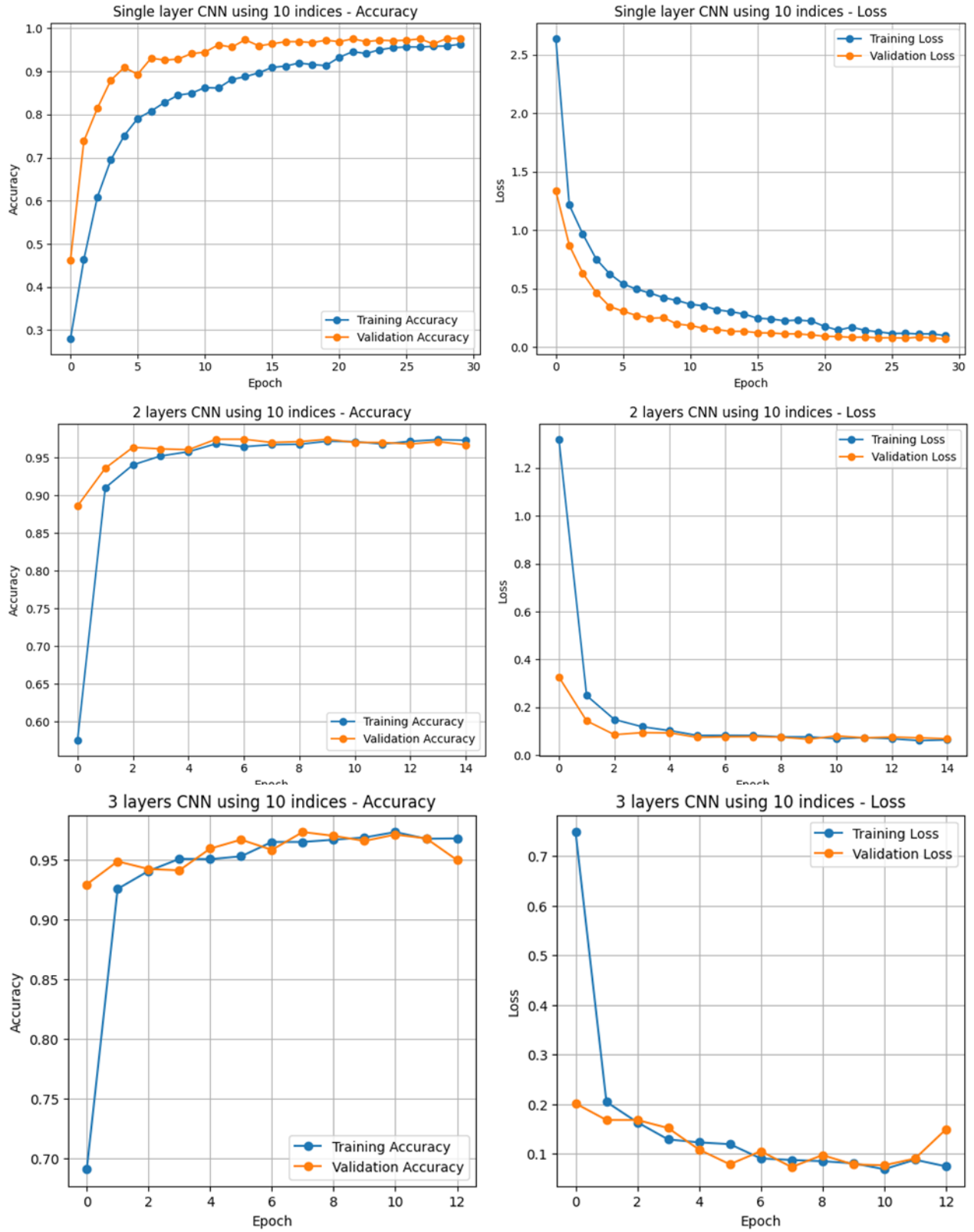


Figure 19: Training accuracy and loss of each CNN model for 10 sweep length time-frequency images.

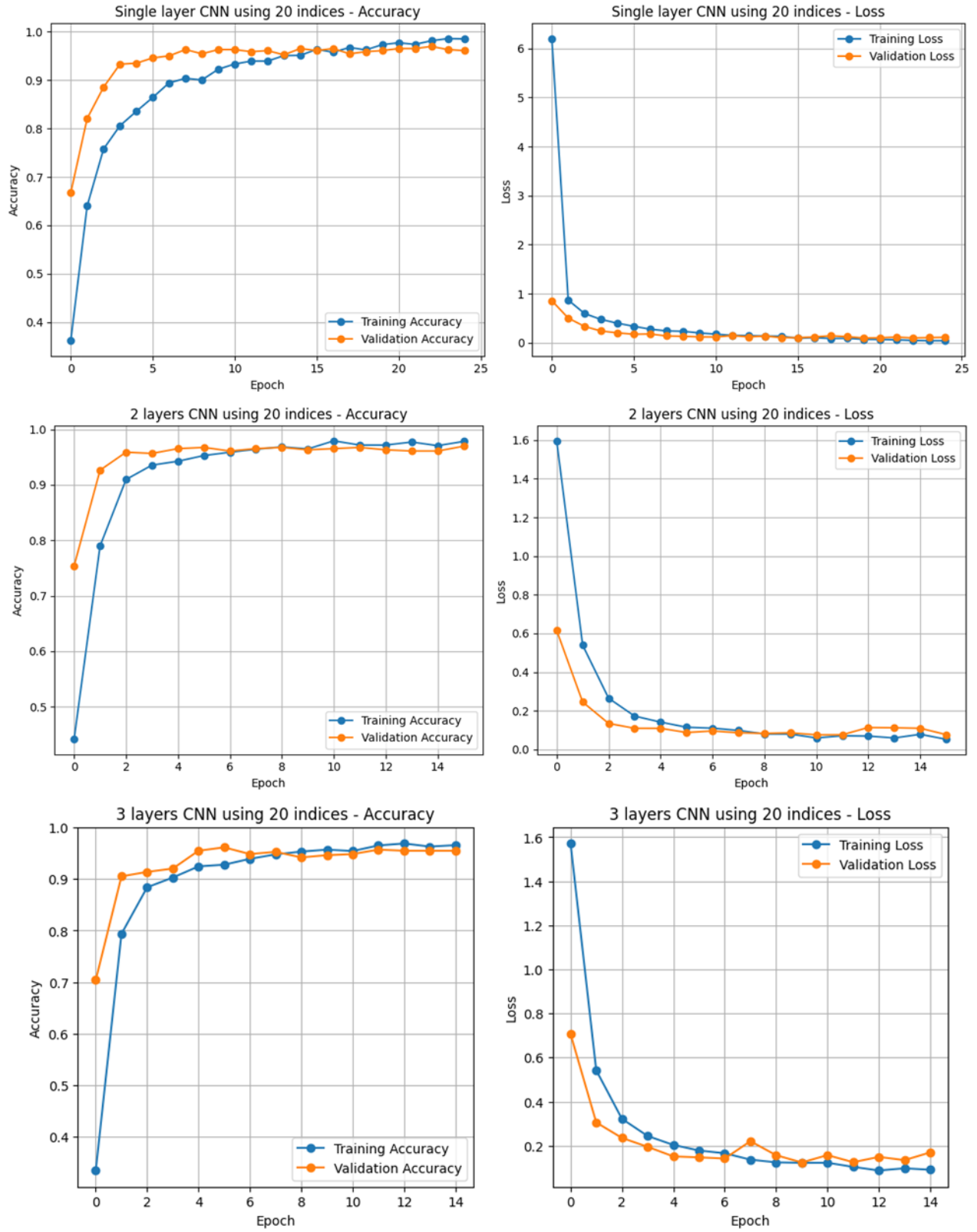


Figure 20: Training accuracy and loss of each CNN model for 20 sweep length time-frequency images.

## Results

### *Linear regression*

The efficacy of a simple linear regression model in predicting volume change was evaluated per resonant frequency index.

TABLE 4

Summary of results from the linear regression models.

Flow Rate (ml/min)	Resonant Frequency Index	R <sup>2</sup> Value	Pearson r	p-value
0	1	0	N/A	N/A
0	2	0	N/A	N/A
0	3	0	N/A	N/A
0	4	0	N/A	N/A
1	1	0.115	-0.192	1.333E-73
1	2	0.604	-0.288	1.503E-166
1	3	0.692	-0.27	3.929E-146
1	4	0.625	-0.277	5.847E-154
2	1	0.167	-0.317	6.691E-203
2	2	0.441	-0.447	0
2	3	0.011	-0.115	4.9E-27
2	4	0.379	-0.132	4.101E-35
4	1	0.011	-0.012	0.2412
4	2	0.209	-0.017	0.08245
4	3	0.029	-0.005	0.5857
4	4	0.163	-0.015	0.1402
5	1	0.02	0.075	1.59E-13
5	2	0.028	0.072	1.579E-12
5	3	0.075	0.094	2.521E-20
5	4	0.047	0.1	6.997E-23

Across all flow rates and resonant frequencies, the highest R<sup>2</sup> value achieved was 0.692, demonstrating that simple linear regression is ill-poised for determining rate change in hematoma growth. Using the first three components of a principal component analysis of the five resonant

frequency shifts in the dataset, multivariate linear regression was evaluated. A mean square error of 2.021 and an  $R^2$  value of 0.013 was achieved, further demonstrating the inability of linear regression models for the use of predicting rate change in hematoma growth

*Machine Learning Models*

The optimal hyperparameter configurations for logistic regression, k-nearest neighbors, and random forest models were determined via a parameter grid search.

TABLE 5

Summary of the parameters explored, the best parameters found, and accuracy associated with the best parameter configuration per model.

Model	Parameters Explored	Number of Combinations	Best Parameters	Accuracy
<b>Logistic Regression</b>	C: [0.1, 1, 10, 100],  Solver: ['lbfgs', 'liblinear', 'newton-cg', 'sag', 'saga'],  Maximum iterations: [1000, 2000]	40	C: 0.1,  Solver: 'newton-cg',  Maximum iterations: 1000	0.31
<b>KNN</b>	Neighbors: [3, 5, 7, 9],  Weights: ['uniform', 'distance'],  Metric: ['euclidean', 'manhattan']	16	Neighbors: 5,  Weights: 'distance',  Metric: 'manhattan'	0.925
<b>Random Forest</b>	Number of estimators: [100, 200, 300],  Maximum depth: [None, 5, 10],  Minimum samples splits: [2, 5, 10]	27	Number of estimators: 300,  Maximum depth: None,  Minimum samples splits: 2	0.943

After finding the best hyperparameter configuration, each model was evaluated by assessing their accuracy in predicting flow rate. The stratified k-folds ( $k = 10$ ) method was employed in order to confidently assess the models' performances. In addition, a confusion matrix and ROC curve plot are included to provide further details on model performance (Figure 21, Figure 22, and Figure 23).

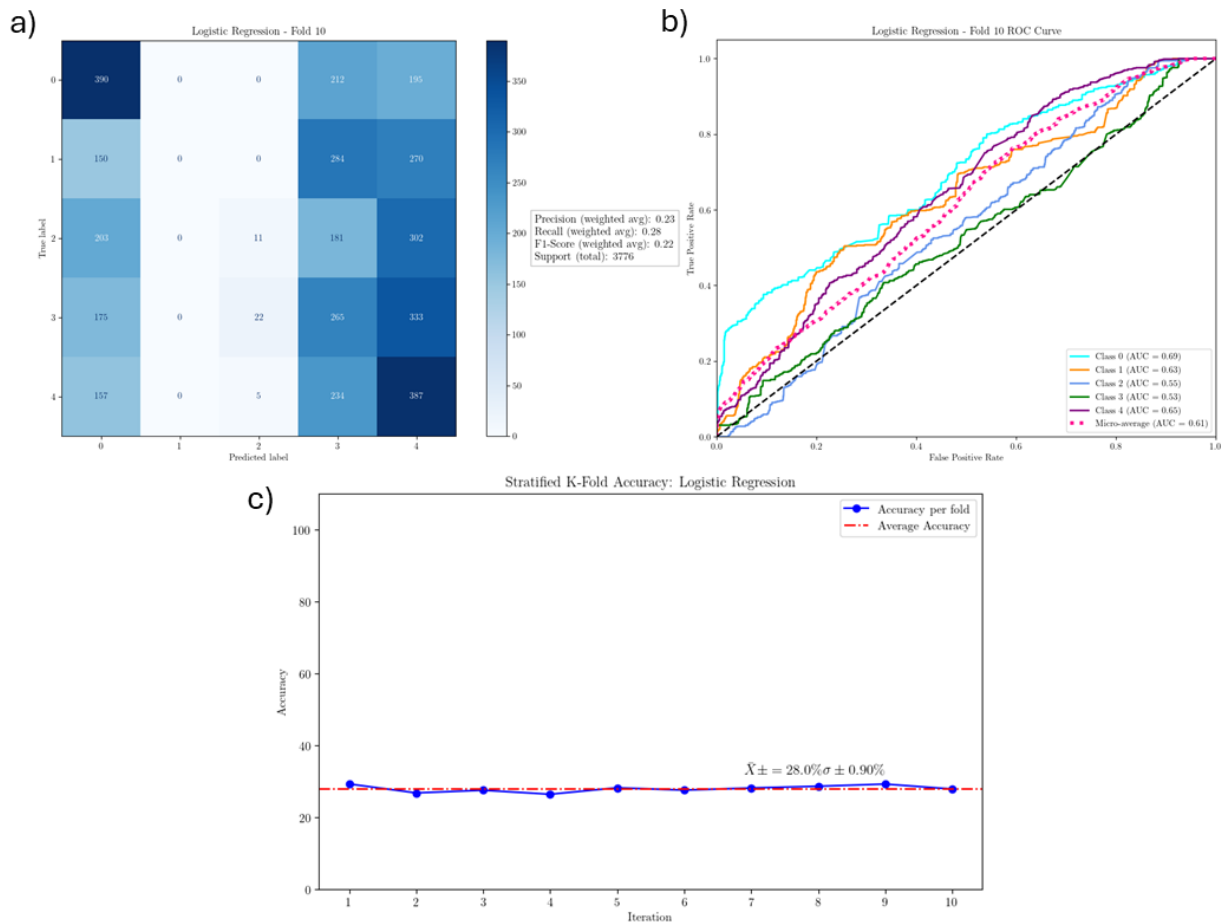


Figure 21: The confusion matrix of the highest performing fold of the logistic regression model (a) and its accompanying ROC curve (AUC = 0.61) (b). The grand mean ( $\bar{X}$ ) and standard deviation ( $\sigma$ ) of the k-stratified fold accuracy ( $k=10$ ) are 28.0% and 0.90%, respectively.

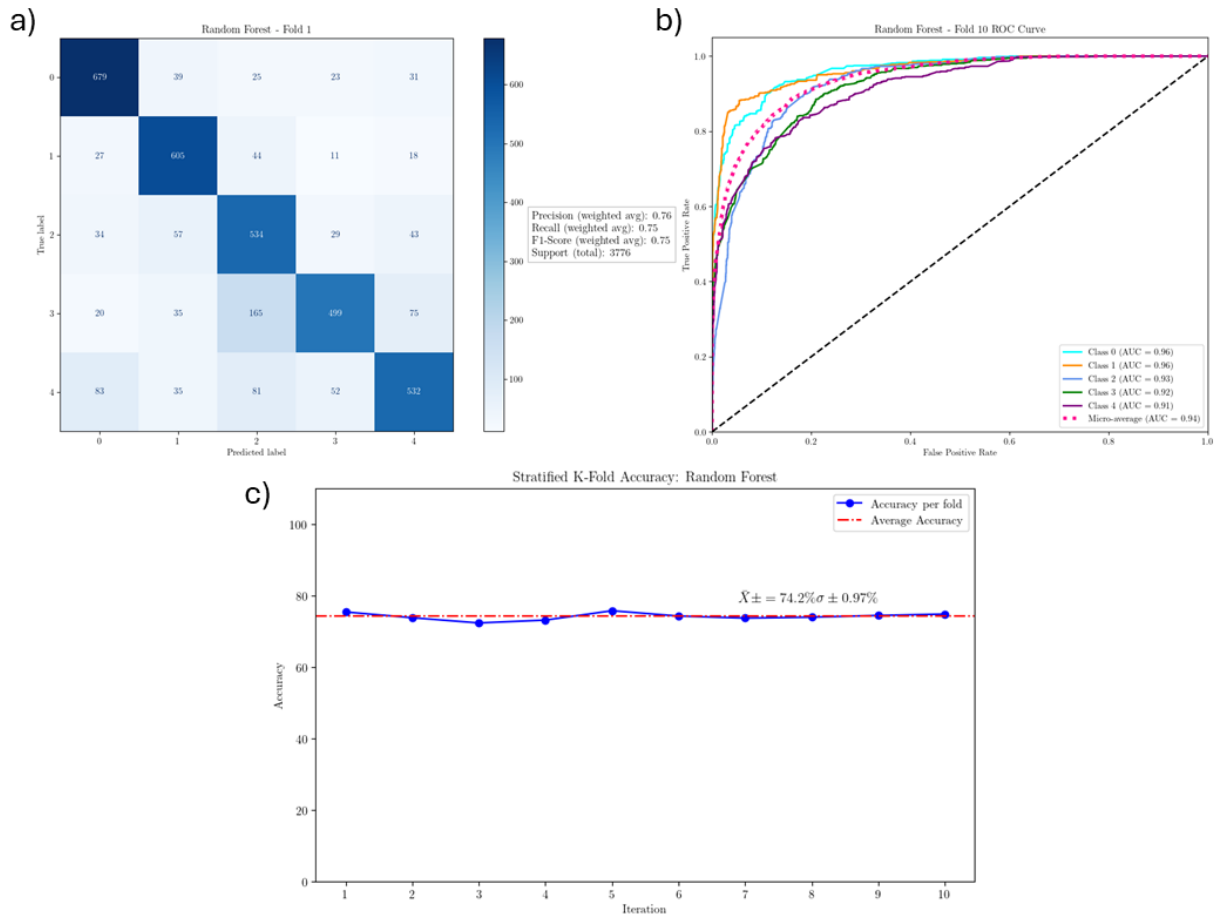


Figure 22: The confusion matrix of the highest performing fold of the random forest model (a) and its accompanying ROC curve (AUC = 0.94) (b). The grand mean ( $\bar{X}$ ) and standard deviation ( $\sigma$ ) of the k-stratified fold accuracy (k=10) are 74.2% and 0.97%, respectively

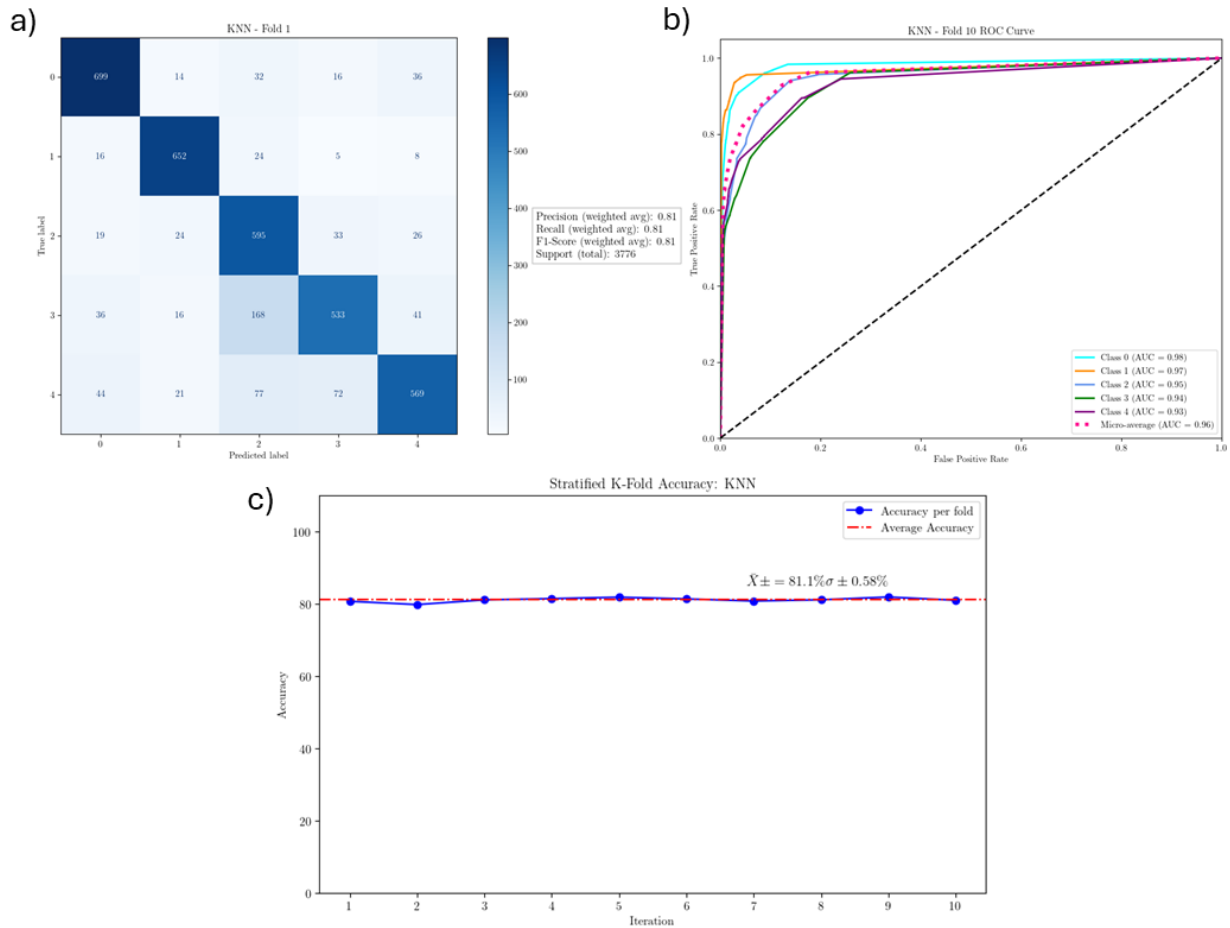


Figure 23: The confusion matrix of the highest performing fold of the KNN model (a) and its accompanying ROC curve (AUC = 0.96) (b). The grand mean ( $\bar{X}$ ) and standard deviation ( $\sigma$ ) of the k-stratified fold accuracy (k=10) are 81.1% and 0.58%, respectively.

### CNN Models

A total of 6 parameter grid searches were conducted in order to find the optimal hyperparameter configuration for the single layer, 2-layers, and 3-layers CNN using both the 10 and 20 sweep length datasets.

TABLE 6

Optimal hyperparameter configuration for the single layer CNN model of both the 10 sweep and 20 sweep length datasets.

Single Layer CNN		
Parameter	10 Sweeps	20 Sweeps
Learning rate	0.001	0.001
Dropout rate	0.2	0.2
Filters	32	64
Dense units	128	128
Batch size	32	16
Epochs	30	30

TABLE 7

Optimal hyperparameter configuration for the 2 layers CNN model of both the 10 sweep and 20 sweep length datasets.

2 Layers CNN		
Parameter	10 Sweeps	20 Sweeps
Learning rate	0.001	0.001
Dropout rate	0.2	0.2
Filters	64	32
Dense units	256	128
Batch size	32	32
Epochs	30	30

TABLE 8

Optimal hyperparameter configuration for the 3 layers CNN model of both the 10 sweep and 20 sweep length datasets.

3 Layers CNN		
Parameter	10 Sweeps	20 Sweeps
Learning rate	0.001	0.001
Dropout rate	0.3	0.3
Filters	32	64
Dense units	256	128
Batch size	16	32
Epochs	30	30

An overview of the performance of each of these model-dataset pairs are given by way of confusion matrices (Figure 24). Predicted and true labels are assessed for each model-dataset pair using a validation subset making up 20% of the total dataset.

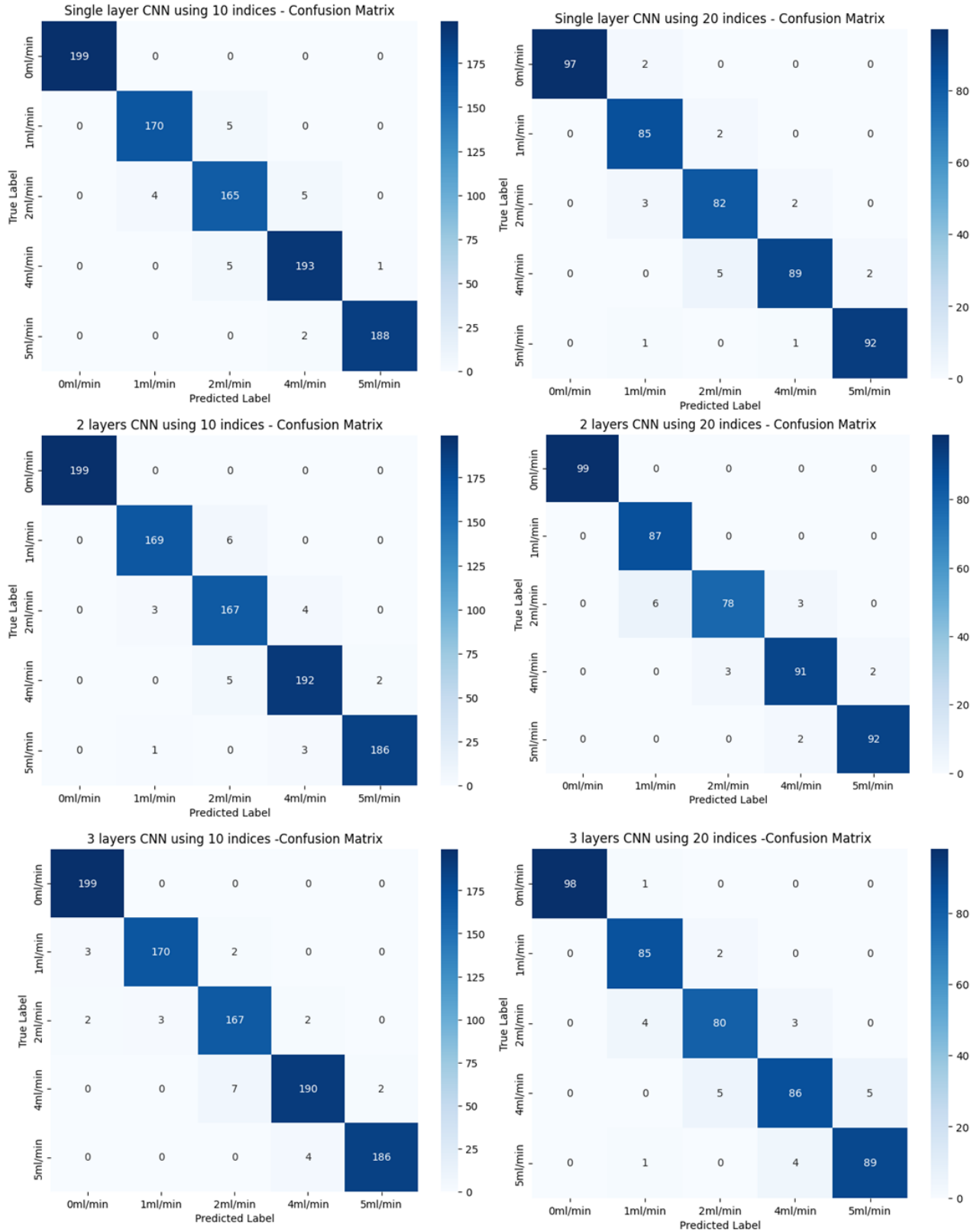


Figure 24: Confusion matrices of each CNN model for both the 10 and 20 sweep length datasets.

The results from the stratified K-fold accuracy plots (Figure 25) and the ROC curves (Figure 26) demonstrate the classification performance of the CNN models in predicting hematoma expansion rates. The accuracy plots indicate that the single-layer CNN exhibits high variability across different folds, with an average accuracy of approximately 74% for both the 10-index and 20-index datasets. This suggests that the single-layer model is less stable and more sensitive to variations in the dataset. In contrast, the 2-layer and 3-layer CNNs achieve significantly higher accuracy, approximately 96%, with minimal variance, highlighting their improved robustness and ability to capture complex features in the data.

The ROC curves show near-perfect classification performance across all CNN models, with AUC values of 1.0 for nearly all classes. This suggests that the models are highly effective in distinguishing between different flow rates. However, such high AUC values may indicate potential overfitting, particularly given the relatively small dataset size. The higher complexity models (2-layer and 3-layer CNNs) do not show a substantial improvement over each other, suggesting that increasing model depth beyond two convolutional layers may not yield further performance gains.

Overall, while the CNN models demonstrate strong classification performance, the high AUC values and the observed stability of deeper models suggest that further validation on larger datasets is necessary to confirm their generalizability.

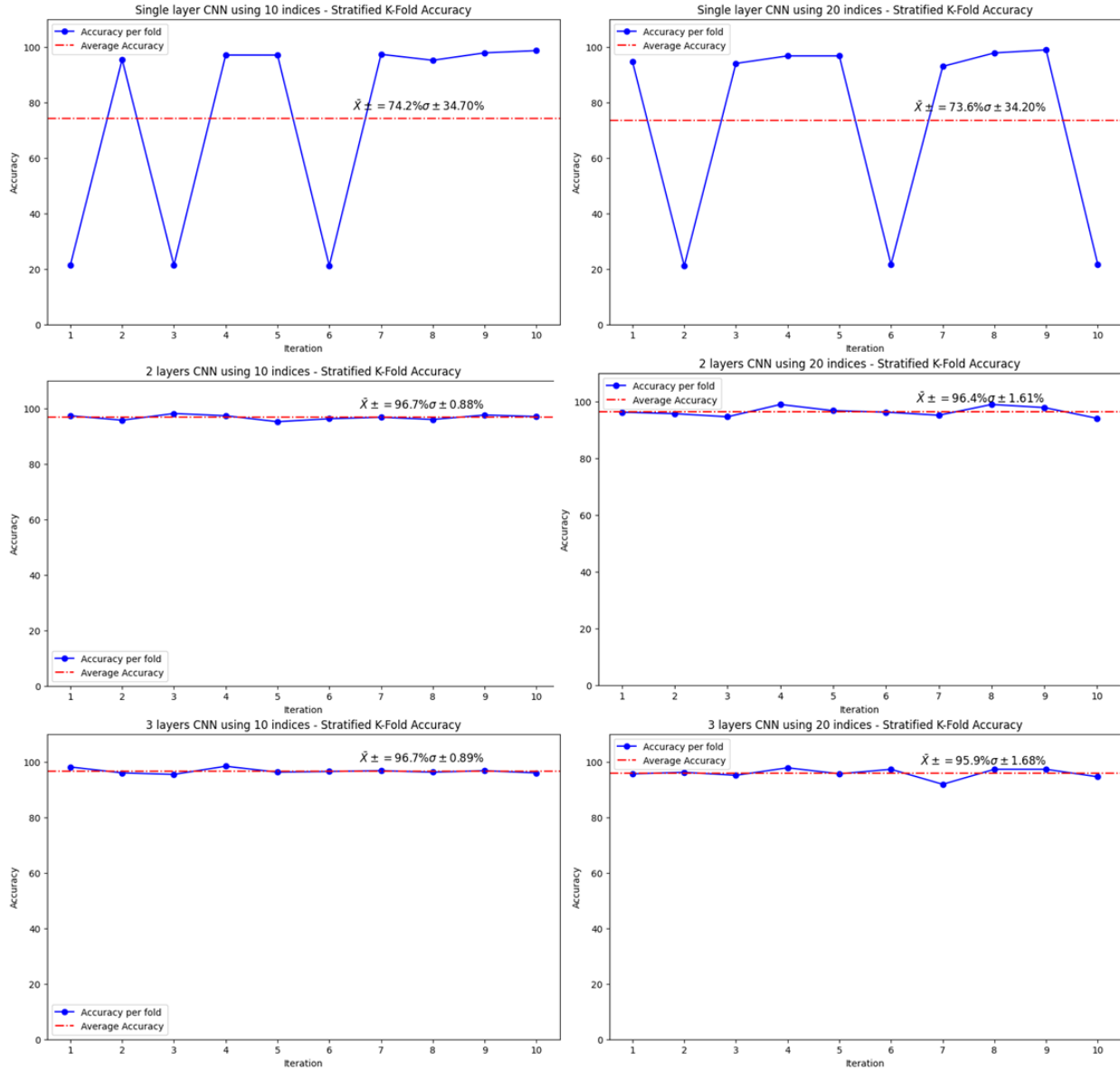


Figure 25: Stratified k-fold accuracy for each CNN model-database pair.

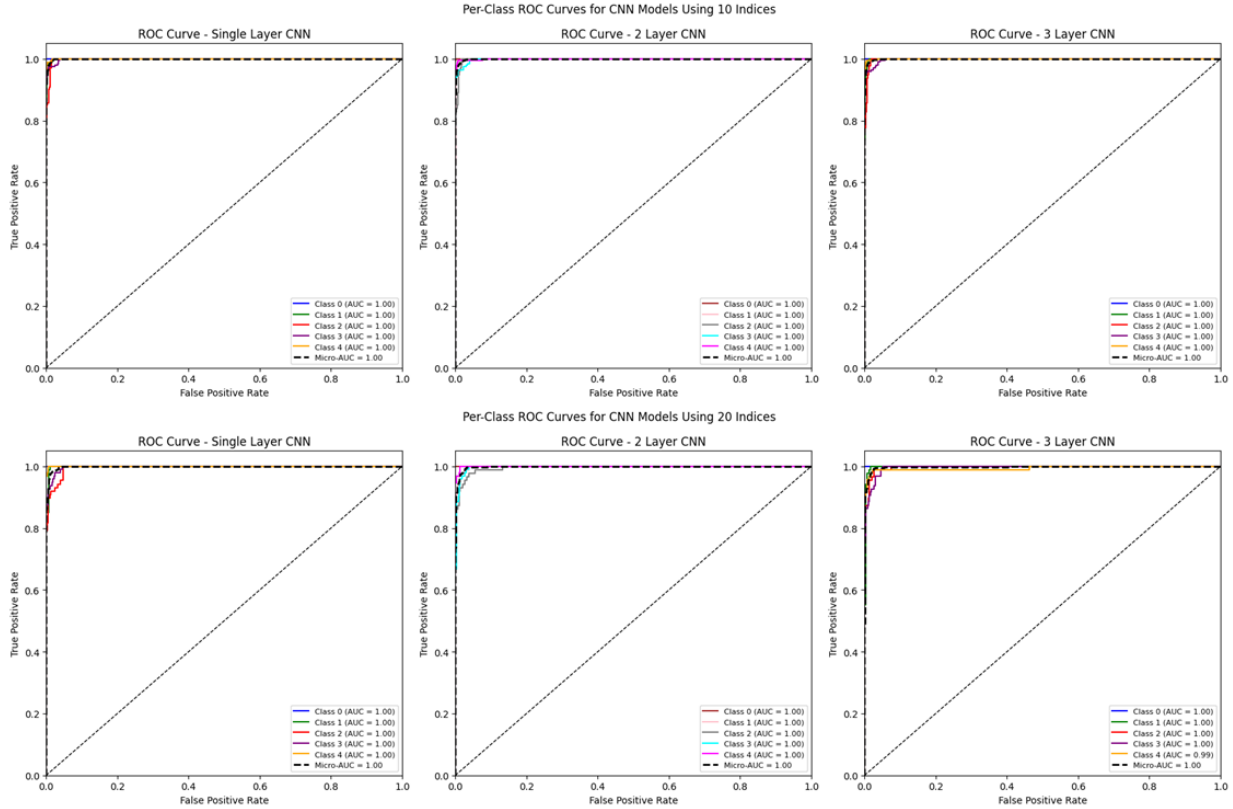


Figure 26: ROC curves for each model-dataset pair.

## Discussion

This study demonstrates the feasibility of using an RF resonator for non-invasive, continuous monitoring of hematoma expansion in a porcine model. The results suggest that this approach could provide a practical alternative to current imaging techniques, such as CT, MRI, and PET, which are often costly, require trained personnel, and are unsuitable for continuous monitoring in emergency settings.

Our results show that linear regression models failed to accurately predict the rate of volume change, with a maximum  $R^2$  value of only 0.692, indicating that the resonant frequency shifts and flow rate demonstrate a degree of non-linearity and requires more complex modeling approaches. Logistic regression performed poorly as well with a grand mean accuracy of 28.0%.

The machine learning models, k-nearest neighbors and random forest, achieved significantly higher classification accuracy in predicting flow rate, with accuracies of 81.1% and 74.2%, respectively. These findings indicate that non-linear machine learning methods outperform traditional regression models for classifying hematoma expansion rates. Additionally, the ROC curve plots do not show evidence of overfitting.

The CNN trained on whole signal, time-frequency images of the magnitude, phase, and imaginary components of the S11 parameter showed promising classification performance. Across the three models (single layer, 2-layers, and 3-layers), the 10-sweep length dataset achieved a higher grand mean accuracy. The 2- and 3-layer CNN models achieved a grand mean accuracy of 96.7%. However, the ROC curves revealed an AUC of 1.0 for each model across both the 10- and 20-sweep length datasets. This is a clear indicator of overfitting and likely demonstrates that the models would not generalize well on unseen data.

Compared to existing techniques, our RF-based method offers several advantages. Unlike CT or MRI, which provide only static images at specific time points, this system can track changes in real-time. Our approach is completely non-invasive and can be used in emergency settings. Additionally, RF resonators and machine learning-based classification require significantly lower infrastructure and resource investment compared to advanced imaging modalities.

Despite these promising findings, several limitations must be addressed before clinical translation. The porcine model used in this study does not fully replicate human tissue properties or actual hematoma expansion patterns, necessitating validation in in-vivo. Environmental and biological variability, including factors such as temperature fluctuations, tissue composition, and individual anatomical differences, could impact the sensor's performance. While the CNN-based

approach demonstrated strong classification performance, a larger sample size will be needed to train a model that is more able to generalize and to prevent overfitting.

Future research will aim to validate these findings in a larger sample size, explore alternative sensor placements, and investigate adaptive deep learning techniques to enhance generalization across different subjects and conditions. Additionally, pretrained transfer learning models should be explored. This study establishes the potential of RF resonators combined with deep learning models for detecting and monitoring hematoma expansion. Our findings highlight the viability of non-invasive, RF-based monitoring systems as a complementary tool to existing imaging techniques. With further refinement, this approach could serve as an accessible, cost-effective, and continuous monitoring solution for early intervention in intracranial hemorrhage cases.

## References

- Alruwaili, Fayez, Kim Cluff, Jacob Griffith, and Hussam Farhoud. 2018. 'Passive self resonant skin patch sensor to monitor cardiac intraventricular stroke volume using electromagnetic properties of blood', *IEEE journal of translational engineering in health and medicine*, 6: 1-9.
- Becker, Ryan. 2019. 'RF resonant skin patch sensor for peripheral limb hemodynamics', Wichita State University.
- Brouwers, H Bart, and Steven M Greenberg. 2013. 'Hematoma expansion following acute intracerebral hemorrhage', *Cerebrovascular diseases*, 35: 195-201.
- Chalet, Lucie, Timothé Boutelier, Thomas Christen, Dorian Raguenees, Justine Debatisse, Omer Faruk Eker, Guillaume Becker, Norbert Nighoghossian, Tae-Hee Cho, and Emmanuelle Canet-Soulas. 2022. 'Clinical imaging of the penumbra in ischemic stroke: from the concept to the era of mechanical thrombectomy', *Frontiers in Cardiovascular Medicine*, 9: 861913.
- Cluff, Kim, Ryan Becker, Balakumar Jayakumar, Kiyun Han, Ernie Condon, Kenneth Dudley, George Szatkowski, Iraklis I Pipinos, Ryan Z Amick, and Jeremy Patterson. 2017. 'Passive Wearable Skin Patch Sensor Measures Limb Hemodynamics Based on Electromagnetic Resonance', *IEEE Transactions on Biomedical Engineering*, PP.
- Griffith, Jacob, Kim Cluff, Brandon Eckerman, Jessica Aldrich, Ryan Becker, Peer Moore-Jansen, and Jeremy Patterson. 2018. 'Non-invasive electromagnetic skin patch sensor to measure intracranial fluid-volume shifts', *Sensors*, 18: 1022.
- Griffith, Jacob L. 2019. 'Non-invasive, point-of-care monitoring of shifts in intracranial biofluid volume using an electromagnetic skin patch sensor', Wichita State University.
- Griffith, Jacob L, Wakim Andre' A, Peer Moore-Jansen, and Kim Cluff. 2016. "Non-invasive biomedical patch sensor to measure intracranial pressure." In *Wearable and Implantable Body Sensor Networks (BSN), 2016 IEEE 13th International Conference on*, 211-11. IEEE.
- Griffith, Jacob L, Kim Cluff, Grant M Downes, Brandon Eckerman, Subash Bhandari, Benjamin E Loflin, Ryan Becker, Fayez Alruwaili, and Noor Mohammed. 2023. 'Wearable sensing

- system for NonInvasive monitoring of intracranial BioFluid shifts in aerospace applications', *Sensors*, 23: 985.
- Ikeme, Shelly, Emilie Kottenmeier, Goldfield Uzochukwu, and Waleed Brinjikji. 2022. 'Evidence-based disparities in stroke care metrics and outcomes in the United States: a systematic review', *Stroke*, 53: 670-79.
- Loflin, Benjamin, Kim Cluff, Jacob Griffith, and Noor Mohammed. 2020. 'Identification of shoulder joint clearance in space suit using electromagnetic resonant spiral proximity sensor for injury prevention', *Acta Astronautica*, 170: 46-54.
- LoPresti, Melissa A, Samuel S Bruce, Elvis Camacho, Sudkir Kunchala, Byron G Dubois, Eliza Bruce, Geoff Appelboom, and E Sander Connolly Jr. 2014. 'Hematoma volume as the major determinant of outcomes after intracerebral hemorrhage', *Journal of the neurological sciences*, 345: 3-7.
- Mohammadshahi, Marita, Mino Alipouri Sakha, Atefeh Esfandiari, Maryam Shirvani, and Ali Akbari Sari. 2019. 'Cost effectiveness of mobile versus fixed computed tomography and magnetic resonance imaging: a systematic review', *Iranian Journal of Public Health*, 48: 1418.
- Mohammed, Noor. 2019. 'A noninvasive, electromagnetic, epidermal sensing system for biofluid phenomena detection', Wichita State University.
- Mohammed, Noor, Kim Cluff, Jacob Griffith, and Ben Loflin. 2019. 'A noninvasive, electromagnetic, epidermal sensing device for hemodynamics monitoring', *IEEE transactions on biomedical circuits and systems*, 13: 1393-404.
- Mohammed, Noor, Kim Cluff, Mark Sutton, Bernardo Villafana-Ibarra, Benjamin E Loflin, Jacob L Griffith, Ryan Becker, Subash Bhandari, Fayez Alruwaili, and Jaydip Desai. 2022. 'A flexible near-field biosensor for multisite arterial blood flow detection', *Sensors*, 22: 8389.
- Nowinski, Wieslaw L. 2024. 'Taxonomy of Acute Stroke: Imaging, Processing, and Treatment', *Diagnostics*, 14: 1057.
- Schmidt, Devin, Anil Mahapatro, Ben Loflin, and Kim Cluff. 2022. 'Evaluation of Polyvinylidene Fluoride (PVDF) integrated sensor for physiological temperature detection', *Materials Technology*, 37: 1725-33.

Szatkowski, George N, Kenneth L Dudley, Laura J Smith, Chuantong Wang, and Larry A Ticatch. 2014. 'Open Circuit Resonant (SansEC) Sensor Technology for Lightning Mitigation and Damage Detection and Diagnosis for Composite Aircraft Applications', *Technical Report: NASA/TP-2014-218554*.

Woodard, Stanley E. 2010. 'Functional electrical sensors as single component electrically open circuits having no electrical connections', *IEEE Transactions on Instrumentation and Measurement*, 59: 3206-13.

———. 2011. "SansEC sensing technology—A new tool for designing space systems and components." In *2011 IEEE Aerospace Conference*, 1-11. IEEE.